NATIONAL AERONAUTICS AND SPACE ADMINISTRATION

Technical Memorandum 33-453

Multispectral Remote Sensing of an Exposed Volcanic Province

J. G. Quade, P. E. Chapman,
and P. A. Brennan
University of Nevada

J. C. Blinn III
Jet Propulsion Laboratory

JET PROPULSION LABORATORY
CALIFORNIA INSTITUTE OF TECHNOLOGY
PASADENA, CALIFORNIA

June 15, 1970

NATIONAL AERONAUTICS AND SPACE ADMINISTRATION

Technical Memorandum 33-453

Multispectral Remote Sensing of an Exposed Volcanic Province

J. G. Quade, P. E. Chapman,
and P. A. Brennan
University of Nevada

J. C. Blinn III
Jet Propulsion Laboratory

JET PROPULSION LABORATORY
CALIFORNIA INSTITUTE OF TECHNOLOGY
PASADENA, CALIFORNIA

June 15, 1970

Prepared Under Contract No. NAS 7-100
National Aeronautics and Space Administration

Preface

The work described in this memorandum was performed by the Space Sciences Division of the Jet Propulsion Laboratory and the NASA Project Office of the University of Nevada.

Acknowledgment

The investigation, as reported in this technical memorandum, was accomplished as a joint effort by the University of Nevada and the Jet Propulsion Laboratory. The authors express gratitude for the support and services provided by the Earth Resources Program Office and the Flight Operations Office at the NASA Manned Spacecraft Center. In addition, the authors express their appreciation for the cooperation of the United States National Park Service at Mt. Lassen, and the ABC Block Company for the use of their Reno facilities. Also, particular appreciation is expressed by the authors to Dr. J. E. Conel for technical support and for the summary from his referenced paper on a portion of the ground-based microwave measurements.

Contents

Contents (contd)

Tables

Figures

Contents (contd)

Figures (contd)

Abstract

During July of 1968 a mission was flown, for a second year, over a volcanic province at Mt. Lassen National Park, in support of the NASA Earth Resources Program. Day and night flights were completed with the following instruments operating satisfactorily: two 9-in. by 9-in. metric cameras with black and white and color IR film, an 8–14 μm IR scanner, four microwave radiometers operating at 8.9, 15.8, 22.2, and 34.0 GHz and a 13.3-GHz radar scatterometer.

Four ground stations were manned during the flights to monitor ground temperatures and moistures. These data were used in conjunction with ground-based radiometers operating at 1.4, 9.3, 13.7, and 37.0 GHz. Prior to the overflights, extensive ground studies (terrametrics), utilizing standard geologic and geophysical techniques, were performed. Some of these studies were reported in greater detail in JPL Technical Memorandum 33-405; however, those pertinent to this report and studies completed this year are reported herein.

Data from the aircraft and ground-based sensors are presented with the relative merits of each sensor discussed along with recommendations for their application.

Multispectral Remote Sensing of an Exposed Volcanic Province

I. Introduction

In support of the NASA Earth Resources Program, a second year of empirical study was conducted in July of 1968 in the vicinity of Mono Lake, Reno, Nevada, and the Mt. Lassen Test Site. The previous study (Ref. 1) concentrated on determining the geologic characteristics of the test site, relating them to the response of the multifrequency microwave radiometers. After this study, it was apparent to the authors that the understanding of the test site and the remote sensing techniques could be significantly increased by performing ground-based microwave radiometric studies and by expanding the study to include the other sensors available on the NASA CV 240A aircraft. These improvements were incorporated and are discussed herein. In particular, this report contains the results of a ground-based microwave radiometer study of the fundamentals relating geologic parameters to microwave radiometric response and individual discussions of the different aircraft sensors, black and white photography, color IR photography, 8–14 μm thermal IR imagery, 13.3 GHz radar scatterometry, and multispectral microwave radiometry. The data from the sensors are then related and discussed in terms of three classes of terrametrics (ground-based studies).

II. Geology

The Mt. Lassen Test Site is part of a volcanic province which contains a well-exposed series of eruptive rocks and a well-formed cinder cone. The site lies about 10 miles east of Lassen Peak in the Mt. Lassen National Park. The cinder cone and lava flows were produced by several thousand years of sporadic eruptions (last active in 1851), separated by long periods of quiescence. The periods of cone building gave rise to basalt flows formed by the effusion of lava from the cone base. Of the several cones on the site, only the largest, at the northwestern edge of the basalt flow, is conspicuous.

The latest lava flows dammed the drainage into Butte Lake, forming Snag Lake, now 33 feet higher than Butte Lake (Fig. 1). Prior to the last flows, diatomaceous earth accumulated in Butte Lake, and vestiges can be found along the margins of the lake and lava flows.

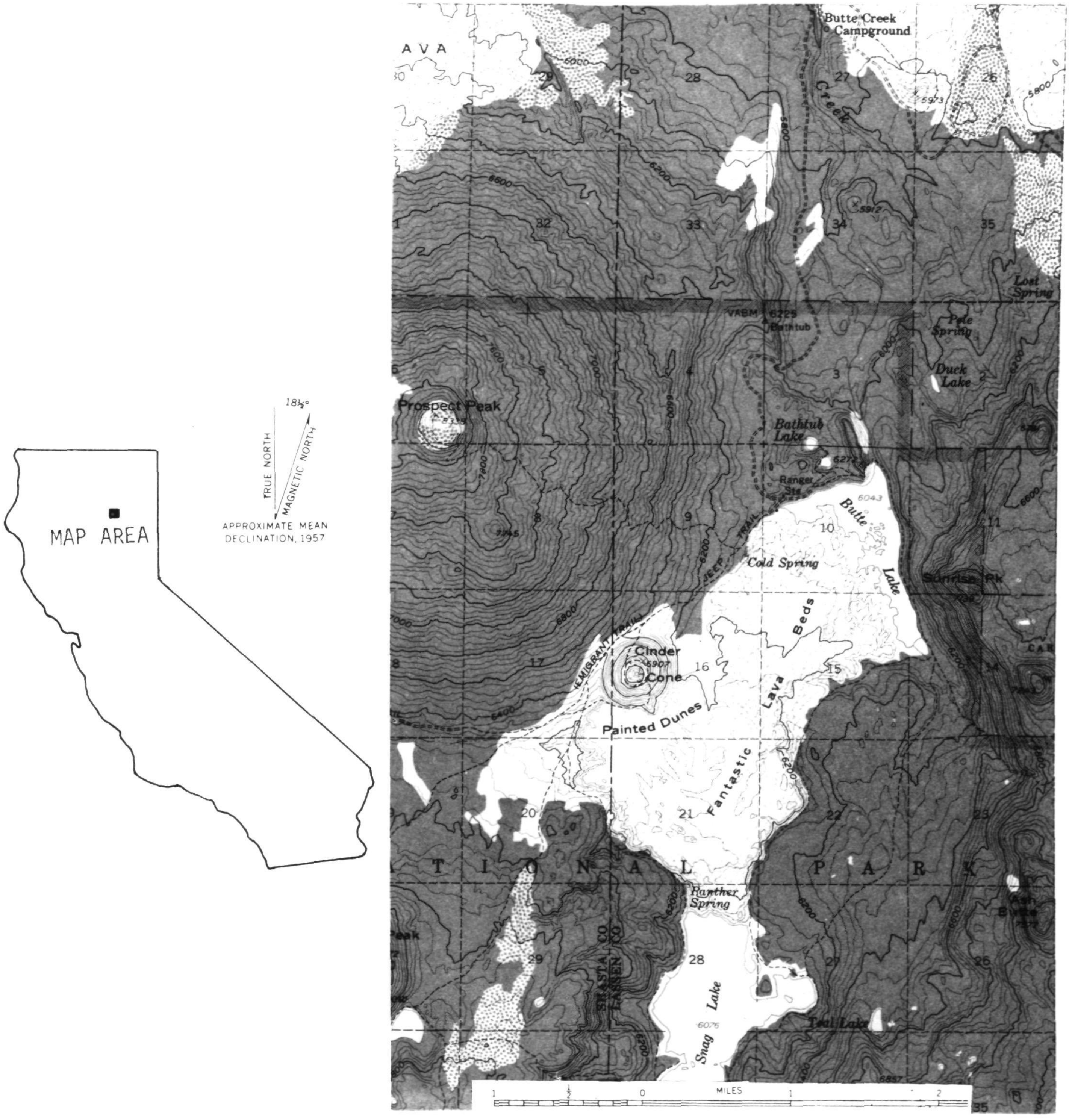

PROSPECT PEAK, CALIF.
N4030—W12115/15
1957

Fig. 1. Index map of the Mt. Lassen Test Site

The test site may be divided into seven basic units. These are illustrated in a photograph of the site (Fig. 2) and the supporting geologic map (Fig. 3). The dark areas, designated as 5 and 6 on Fig. 2, consist mainly of blocky lava, some aa, and less pahoehoe, the latter being associated with the later flows. The last flow (area 6), which is distinctly black, can be easily traced from the breach in the south side of the cone. Pumaceous cinder covers the immediate vicinity of the cinder cone. The altered cinder (area 4) is the result of hydrothermal waters, moving upward from the hot lava flows. Cinder that did not fall upon the hot lava (area 3) shows little or no alteration and remains dark gray to black. Lava material along both flight lines is nearly homogeneous in texture and composition.

A. Petrology and Geochemistry

The recent volcanic flows consist of dark basalts with olivine and plagioclase phenocrysts in a groundmass of plagioclase, pyroxene, magnetite, ilmenite, and glass. Much of the basalt contains quartz inclusions, ranging in size from a millimeter to several centimeters. The inclusions are irregular, anhedral, crystals or polycrystalline aggregates, surrounded by a microcrystalline zone composed of radiating laths of pyroxene and feldspar. These quartz inclusions may be the result of assimilation of diatomite from the lake bottom, over which the basalts flowed.

Detailed studies of the rock chemistry indicate only small variation in the chemical makeup of the lava and cinder. The chemical consistency between cinder and lava eliminates the compositional parameter from affecting the sensor data. The chemical results are summarized in Table 1. The high silica content of the basalt (55%) is due to the quartz inclusions. The true basalt, as erupted, probably contained no more than 52% to 53% SiO_2. The lower silica content of the altered cinder probably reflects the original composition.

B. Moisture

The cinder field contains considerable moisture at depth; however, the first few feet are relatively dry, due to the dehydrating effects of high daytime surface temperatures. Table 2 shows the average moisture of the cinder fields at the time of overflight.

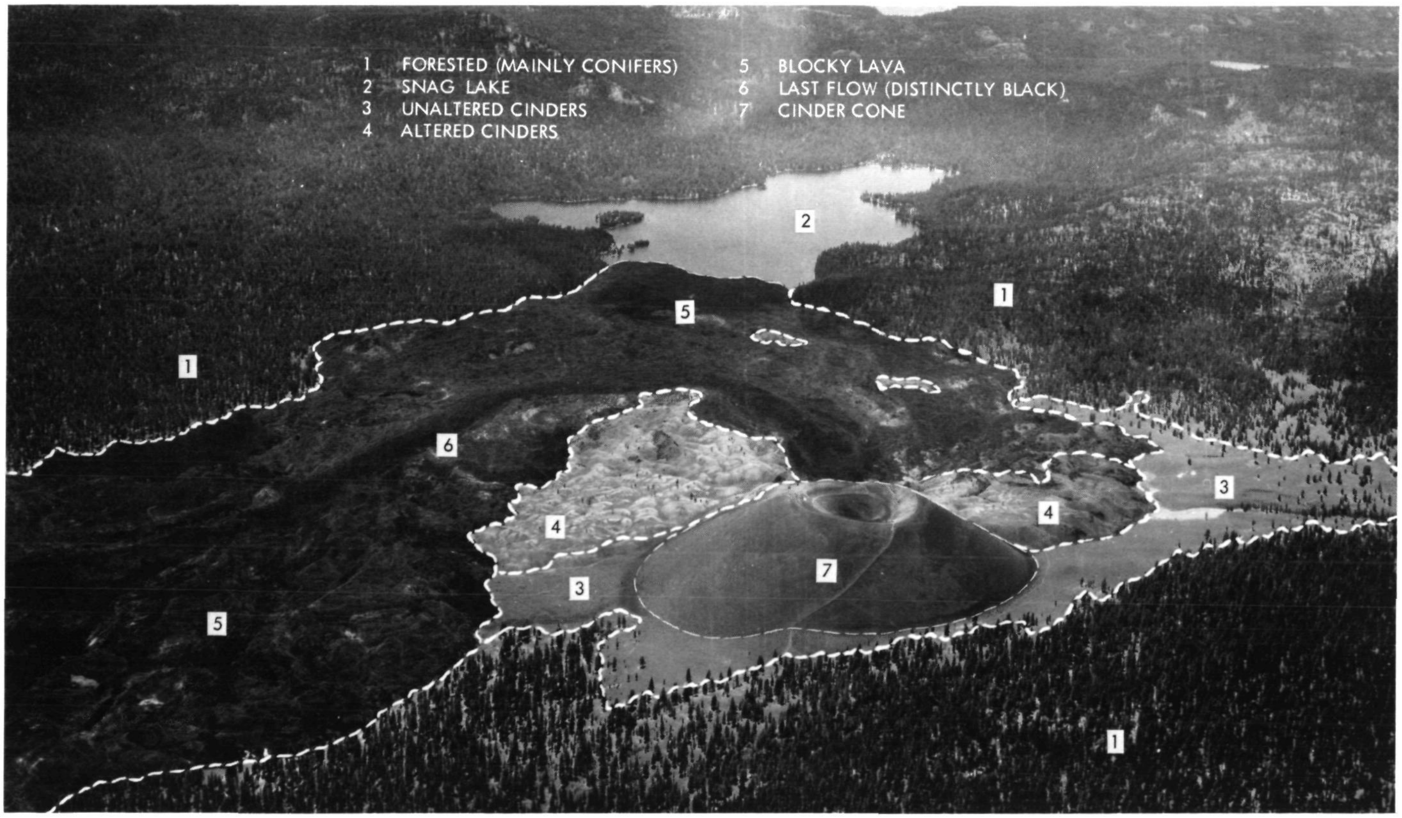

Fig. 2. Aerial view of test site area

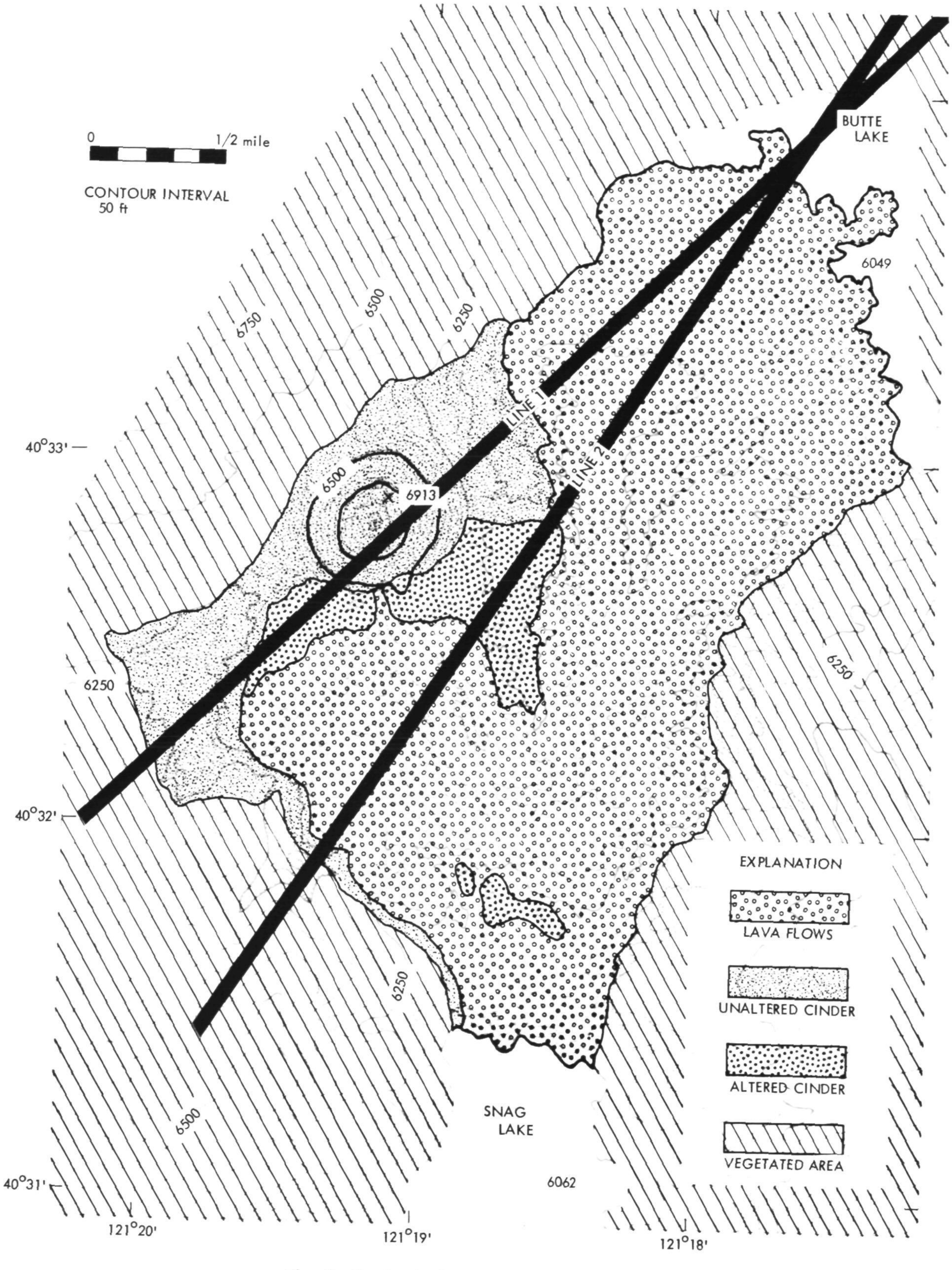

Fig. 3. Geological map of test site area

C. Particle Size and Density

The lava consists of large blocks of material, 30 to 60 cm in diameter. The cinder is composed of scoriaceous pebble-size material. Figure 4 shows the mean particle size distribution of a number of cinder samples.

Table 1. Mean chemical analysis as weight percentage of oxides

Oxides	Basalt flows, %	Weight, %	
		Unaltered cinder	Altered cinder
SiO_2	55.5	55.25	53.68
Al_2O_3	15.67	14.55	13.62
K_2O	1.49	1.48	1.29
CaO	9.64	9.21	9.83
TiO_2	0.79	0.80	0.78
FeO	5.91[a]	5.76[a]	3.72[b]
Fe_2O_3	1.64	1.60	4.13
MgO	8.22	8.33	9.06
Na_2O	3.12	3.02	2.44
Totals	102.03	100.00	98.55

[a] $Fe^{+2}:Fe^{+3}$ ratio assumed to be 4:1.

[b] $Fe^{+2}:Fe^{+3}$ ratio assumed to be 1:1.

The dense lava samples have a density of 2.59 g/cm³ which corresponds to a porosity of approximately 4%. Much of the basalt has a rather high density, though all gradations from very dense basalt to scoriaceous material exists.

The mean cinder density is 1.10 g/cm³; this corresponds to 57% porosity. The cinder density falls into a rather narrow range, between 0.84 and 1.34 g/cm³.

D. Depth Probe Sensing

Shallow seismic work was conducted on both the basalt and cinder, to determine the depths of discontinuities. These studies failed to show either bedrock or

Table 2. Moisture content of cinder

Depth, in.	Midday avg moisture, %	Predawn avg moisture, %
0–½	0.05	0.16
2	0.21	0.12
6	2.59[a]	2.24[a]
8–12	5.24[a]	4.18[a]

[a] Large variations are probably due to slightly different sample locations.

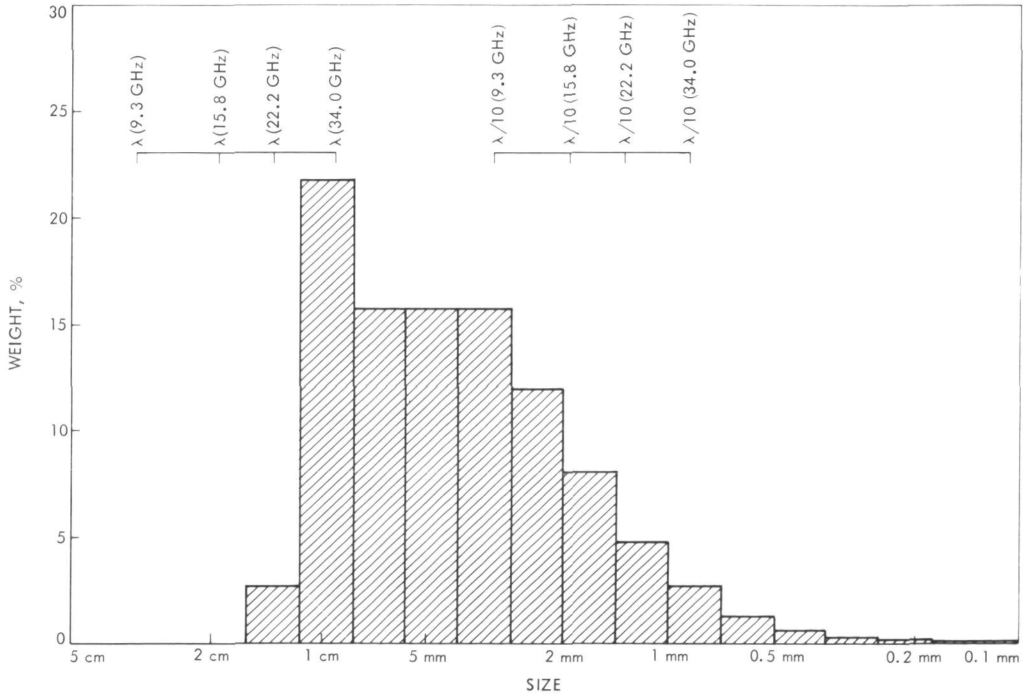

Fig. 4. Cinder grain-size distribution and comparison with radiometer wavelengths

significant vertical change in any of the sampled areas, to a depth of 2–3 ft in the cinder.

III. Flight Summary

As a result of the previous work on the test site, two new flight lines were selected which originate at a point on the west shore of Butte Lake. One of the flight lines runs southwest across the flows and over an altered cinder area crossing geologic units on relatively flat terrain. The other line crosses east to west over the top of the cinder cone. Six runs were flown over each line at an altitude of approximately 2200 ft above ground level. A summary of the flight and the data obtained is contained in Table 3.[1]

IV. Photography

Wild RC-8 metric cameras with 9-in. by 9-in. formats and 6-in. focal length lenses were used for the black and white and the color IR photography. Camera No. 1

Table 3. Aircraft flight summary

Flight	Line	Run	Reconofax IV	Microwave Radiom 62–64	Scatterometer, 13.3 GHz	RC-8 No. 1	RC-8 No. 2
4[a]	1	1	X	10 V	X	Plus X	Color IR
		2		10 H			
		3		45 V			
		4		45 H			
		5		30 V			
	1	6		30 H			
	2	1		10 V			
		2[b]		10 H			
		3		45 V			
		4		45 H			
		5		30 V			
		6		30 H			
4	2	7		10 H		Plus X	Color IR
5[c]	1	1		10 V		–	–
		2		10 H		–	–
		3		45 V		–	–
		4		45 H		–	–
		5		30 V		–	–
		6		30 H		–	–
		1		10 V		–	–
		2		10 H		–	–
		3		45 V		–	–
		4		45 H		–	–
		5		30 V		–	–
5	1	6	X	30 H	X	–	–

[a] Flight 4 commenced at 1125 h and ended at 1230 h PDT on July 18, 1968. The altitude was 2200 ft and the length of each line was 4 mi.

[b] This run was aborted and then repeated. See Line 2, Run 7 of Flight 4.

[c] Flight 5 commenced at 0300 h and ended at 0430 h PDT on July 19, 1968. The altitude was 2200 ft and the length of each line was 4 mi.

---

[1] V and H as used in this table, and elsewhere in this report, refer to vertical and horizontal polarizations respectively.

contained black and white plus X film and camera No. 2 was loaded with Kodak Ektachrome Infrared Aero film, type 8443, with a Wratten No. 12 filter. The flight elevation of 2200 ft above the terrain and an 8.5 s intervalometer setting, produced photographs with a scale of 1:4,500 and a 30% overlap.

A. Black and White Photography

In lieu of boresight cameras slaved to each of the instruments, the black and white photography was used to establish the actual flight tracks. For topographic studies the T-11 black and white camera photography from the previous mission was used, because of the more desirable 60% overlap.

Identification and mapping of lithologic units was done by combining observations of the overall albedo and the topographic expression. Rapid assessment of the topography was made, using successive photographs viewed in stereo. Quantification of the topography, in the form of profiles and topographic maps, was produced using a parallax bar and a Kelch Plotter, after elevations of a few critical points were established. An example of a detailed topographic map compared to a stereoscopic pair is shown in Fig. 5.

In order to fully understand tones on aerial photography, some knowledge of solar energy and the reflective properties of rocks is necessary. A large portion of the incoming solar energy is concentrated in the visible and near IR portion of the spectrum. The incoming radiation is either reflected or absorbed. The reflected energy is directly correlative with the photographic behavior of the target. Albedo is a measure of this reflectivity, and is the single lithologic parameter affecting the photographic systems. Table 4 shows the environmental variables which determine the albedo.

Rocks and soils, because they are mixtures of many differently colored minerals, tend to have gray, brown or reddish colors. Curves produced by a spectrometer of the percent reflectivity of various units tend to be parallel and cross infrequently in the visible spectrum. The visual albedos can be correlated directly with the shade of gray on black and white photographs.

Figure 6 shows the albedos of the three major lithologic types at the Mt. Lassen test site. These data were taken with an ISCO model SR spectroradiometer, which measures light intensity at any desired wavelength. By sampling both the intensity of the incoming light and the reflected light, at 0.005 or 0.01 μm intervals, albedo may be calculated and plotted.

Table 4. Surface characteristics affecting photographic characteristics

Parameters affecting total signal	Environmental variables
Multispectral albedo	Colors of dominant minerals (reflected light)
	Weathering characteristics of rock and soil
	Bulk iron and FeO/Fe_2O_3 ratio in surface skin
	Grain size distribution
	Surface roughness
	Vegetation cover (grass, lichen, etc.)
Multispectral albedo	Moisture (standing water and soil saturation)

B. Near Infrared Photography

The principal use of IR film was to photograph vegetation, and determine its density and vigor. For some sensors, the presence of vegetation complicates the interpretation of geologic parameters, thus, the screening effect of the vegetation must be known. Some geologic parameters may be derived, or inferred directly from vegetation, for a given plant often prefers a given soil chemistry, drainage, or moisture content, etc. Foliage, in general, has a much higher reflectance in the IR portion than in the visible portion of the spectrum. Accentuation of this high reflectance, using IR film, can differentiate varieties of foliage, giving clues to the underlying geology. Thus, the use of IR photography provides a unique way to assist in the differentiation of geologic parameters.

A vegetation density map was produced by plotting the estimated densities near the centers of photos on a 1:24,000 scale map. Each area supports its own characteristic botanical assemblage, visible on the IR photography. Table 5 lists the observable vegetation.

The color IR photographs enhance the altered cinder area because of the low reflectivity of the cinder in the violet, blue, and blue-green region, with relatively high reflectivity in the yellow-green to IR region. Three distinct tones may be seen on the color IR film:

(1) Dark blue-green.

(2) Yellow-orange.

(3) White.

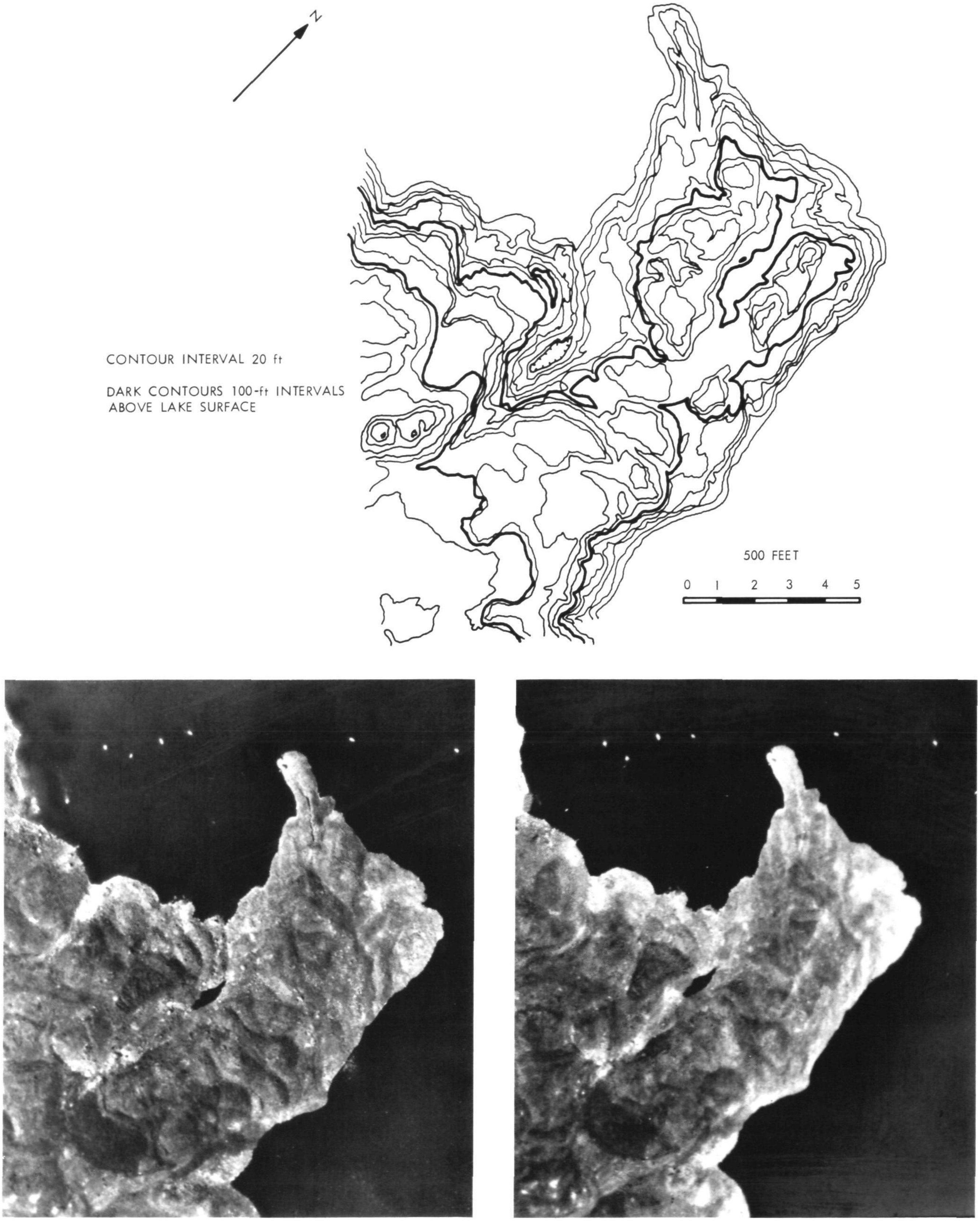

Fig. 5. Detailed topographic map and stereoscopic photographs

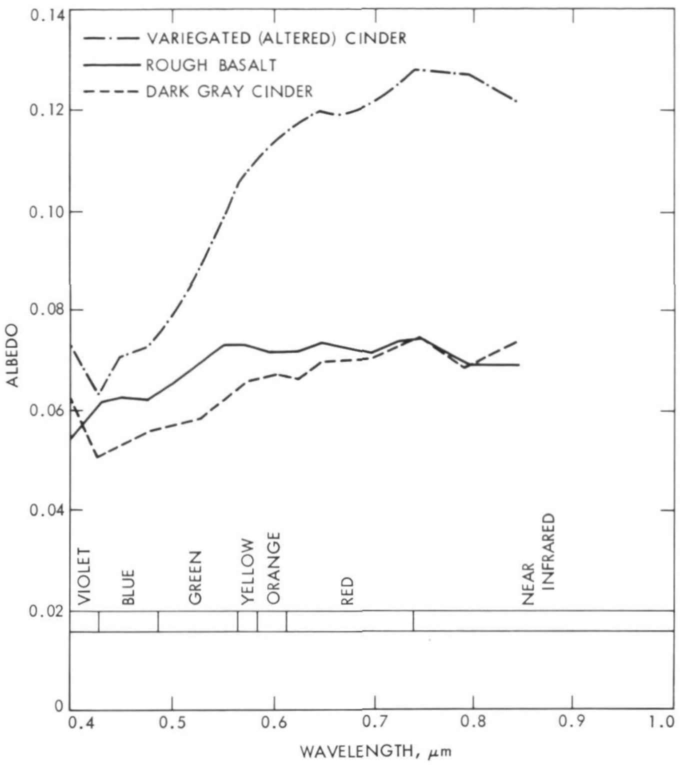

Fig. 6. Albedo curves of major lithologic units

Only grays, tans, and dull reds can be seen on normal color photography. The dark blue-green tone corresponds to areas of gray and olive cinder. Because of low, overall, albedo and its slight reflectance-peak in the yellow-green area, this cinder appears as a dark blue-green on the film. The areas of yellow-orange response on the IR photographs are actually deep red in color with highest reflectivity in the far red almost at the response limit of the human eye and normal film. The high reflectance in that portion of the spectrum corresponding to yellow-orange in the color-shifted film yields the bright orangish color. The white tone is produced by a variegated cinder which is composed of fragments of all colors of gray, green, orange, brown, and red. This material has a light tan appearance from a distance, but has the highest reflectivity of any rock unit over the entire portion of the spectrum to which the IR film is sensitive. The result is an overexposure; a white tone on the photograph.

Table 5. Area distribution of botanical species

Area	Vegetation	Response on color IR photos
Water	Floating plants	Orange to dull pink to yellow-green
	Algae	Royal blue
Shore line	Shore line shrubs and grasses	Bright magenta
	Deciduous trees	Bright red
Diatomite	Coarse grass	Dull magenta
	Very sparse conifers	Dull pink
Altered cinder	Very sparse conifers	Dull pink
Cinder	None to dense conifers	Dull pink
Basalt flows	None	

V. Infrared Imagery

A. General

The Reconofax IV IR imager records the thermal radiation of the surface at wavelengths between 8 and 14 μm. The surface temperature is dependent on a number of physical and meteorological variables. During the daily heating period the surface temperature is regulated by the albedo and thermal diffusivity of the material. The thermal diffusivity, κ, is equal to:

$$\kappa = \frac{K}{c\rho}$$

where K = thermal conductivity
c = specific heat
ρ = density

Thermal diffusivity controls the ability of the material to transfer heat from the surface to subsurface areas and from a depth to the surface after the solar heating period. For example, the basalt may receive more solar energy (due to its low albedo), but, its surface will not heat as rapidly as the cinder (due to its ability to conduct thermal energy downward and store it at depth). Conversely, during the cooling period, the basalt will conduct energy upward to its surface and remain warmer than the cinder.

The thermal diffusivity is measured in the laboratory using cores of rock. A high temperature source is applied to one end of the rock core and the temperature of the other end is monitored. The rate of heating (slope of the line) is proportional to the thermal diffusivity, when the monitored temperature range is small in comparison to the difference between original rock temperature and that of the high temperature source. The results

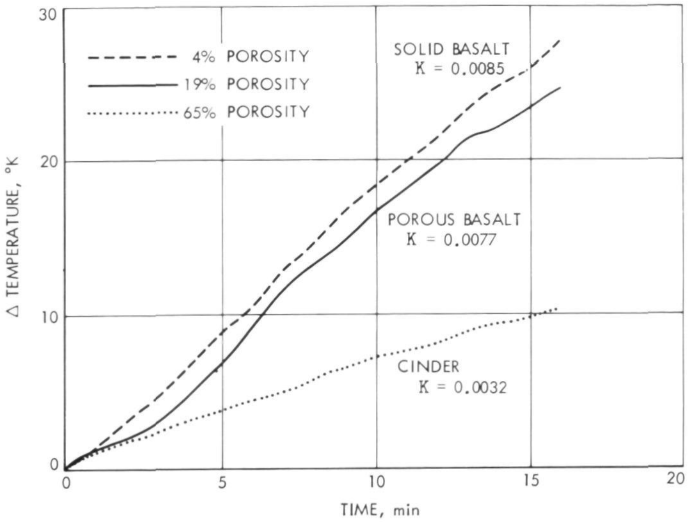

Fig. 7. Thermal diffusivity of basalt and cinder

are plotted in Fig. 7. Absolute thermal diffusivities are computed by comparing these curves with those of materials with known diffusivities. The thermal diffusivities of the basalt and cinder are summarized in Table 6.

Albedo is the percent reflectivity of a material in the visible and near IR portion of the spectrum, in which a majority of the incoming solar radiation is concentrated. Albedo for a given wavelength may be computed from:

$$a_\lambda = \frac{R_\lambda}{I_\lambda}$$

where

a_λ = albedo

R_λ = reflected radiation flux

I_λ = incident or incoming radiation flux

By examining the three main lithologic units at the Mt. Lassen test site (the basalt flows, the gray cinder, and the altered cinder), the relative contributions of albedo and thermal diffusivity by day and by night may be seen. Thermal diffusivity dominantly influences predawn temperatures. The eight hours of darkness prior to the flight eliminates any effect of dissimilar albedos. Both gray cinder and altered cinder are the same temperature, demonstrating this predawn temperature independence of albedo.

Midday temperatures on the Mt. Lassen Test Site also show a strong dependence on thermal diffusivity, however, they are definitely modified by dissimilar albedos. Because of the wide range of thermal diffusivities and a narrow range of albedos, thermal diffusivity plays a dominant role in controlling rock temperature. Figure 8 shows the relationship of temperature to albedo and thermal diffusivity.

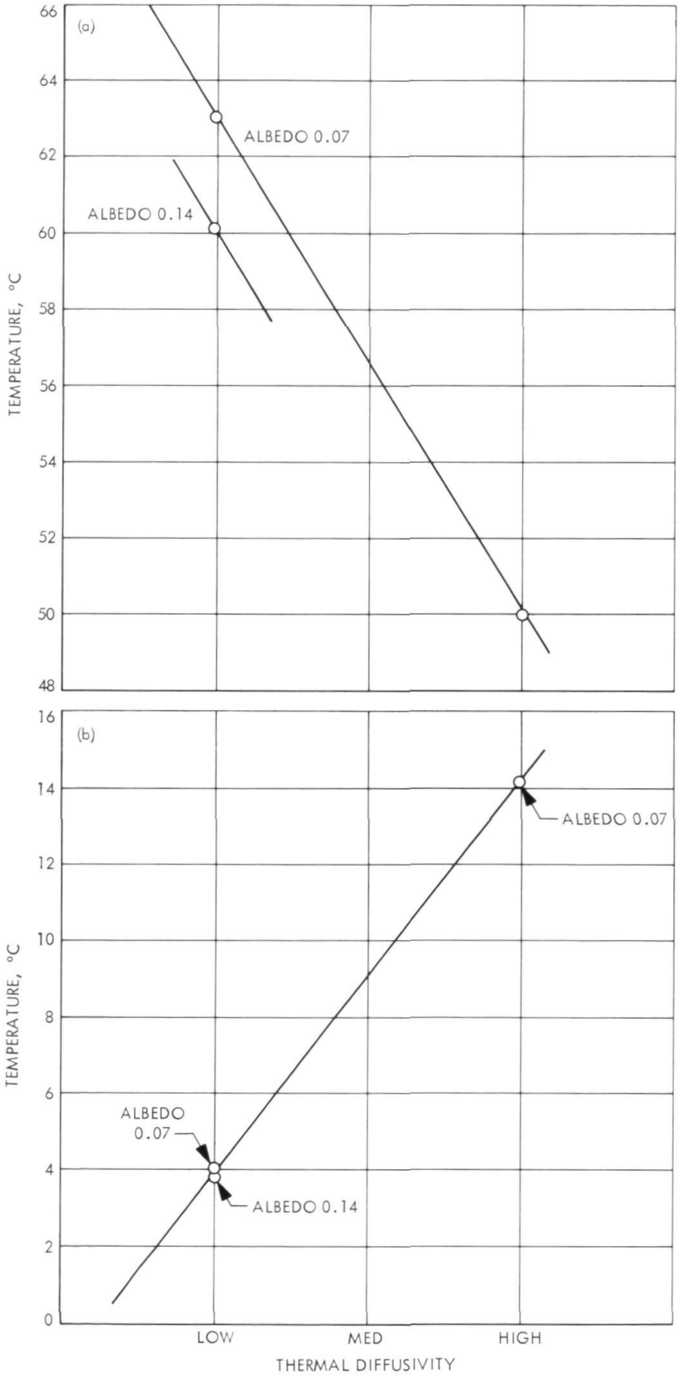

Fig. 8. Effect of thermal diffusivity on IR (surface) temperatures: (a) Midday, (b) Predawn

Table 6. Thermal parameters of major units

Material	Density (ρ), g-cm^3	Porosity[a], %	Thermal diffusivity K, cm^2/s	Specific heat[b] c	Thermal conductivity K, cal/cm/s, °C	Albedo α	Midday temp., °C	Predawn temp., °C
Basalt	2.59	4	0.0085	0.206	0.0045	0.07	50	14
Basalt	2.18	19	0.0070–0.0077	0.206	0.0031–0.0035	0.07	–	–
Basalt	0.71	74	0.0042	0.206	0.0006	0.07	–	–
Cinder, gray	1.09	60	0.0030	0.206	0.0007	0.07	–	–
Cinder, gray	1.10	59	–	0.206	–	0.07	63	4
Cinder, gray	0.95	65	0.0032	0.206	0.0006	0.07	–	–
Cinder, altered	1.10	59	–	0.206	–	0.14	60	4

[a] Calculated assuming solid density of 2.7 g-cm^3.

[b] Computed using Kopp's rule from chemical data.

A third variable, emissivity, controls the amount of energy emitted by the surface of a material. It is a measure of the relative contributions of radiance due to physical temperature and the reflected radiance from the sky and surrounding objects. The higher the emissivity, the greater the role of the physical temperature on the sensed IR signal.

The emittance characteristics of the lava and cinder were measured in the laboratory, with an emissivity chamber constructed at the University of Nevada. The instrument consists of a Barnes Portable Radiation Thermometer (PRT), mounted on top of the emissivity chamber. The lower surface of the chamber is the target material. The upper surface is easily changed from a black body (aluminum coated with 3M Coveral, black, $e_b = 0.98$) to a reflector (gold-plated surface mirror, $e_m = 0.02$). The temperature of the coated aluminum lid is maintained at a higher temperature than the surface under investigation. Thus, increasing reflectivity of the target results in a larger difference between the readings obtained with the black body and with the reflector.

Theoretically, using the temperature readings given by the Barnes Radiometer, the radiant power received $W(T)$ by the Barnes PRT-4 can be calculated as follows:

$$W(T) = \int_{8}^{14} Q(\lambda) B(T, \lambda) \, d\lambda$$

where $Q(\lambda)$ is determined by the spectral transmission of the Barnes PRT-4 filtering system and $B(T, \lambda)$ is Planck's function determined by the temperature T. The emissivity of the target surface e_λ is determined experimentally from the following equation:

$$e_\lambda = \frac{1 - [W(T_{sb}) - W(T_{sm})]}{e_b W(T_b) - e_m W(T_m) + r_b W(T_{sb}) - r_m W(T_{sm})}$$

where $e_b = 0.98$, $r_b = 0.015$, $e_m = 0.02$, $r_m = 0.99$ and m is the mirror surface, b is the black emitting surface, sm is the target surface under the mirror and sb is the target surface under the black emitter. Table 7 shows the emissivity of major rock units at Mt. Lassen.

B. Infrared Data

The midday thermal imagery shown in Fig. 9a indicates a high thermal contrast between water and cinder (the cinder at 60–63°C, and water at 15°C); the rock is at an intermediate temperature. The water with its high thermal inertia remains relatively cold throughout the day and at a fairly constant temperature (day to night variations of approximately 2°C). The basalt flows with their relatively high thermal diffusivity remain cooler than the cinder (which has a higher albedo).

Table 7. Infrared emissivity of major rock units

Rock type	Emissivity, e_λ
Altered cinder, sample 1	0.96
Altered cinder, sample 2	0.95
Rough lava	0.95
Smooth lava	0.92

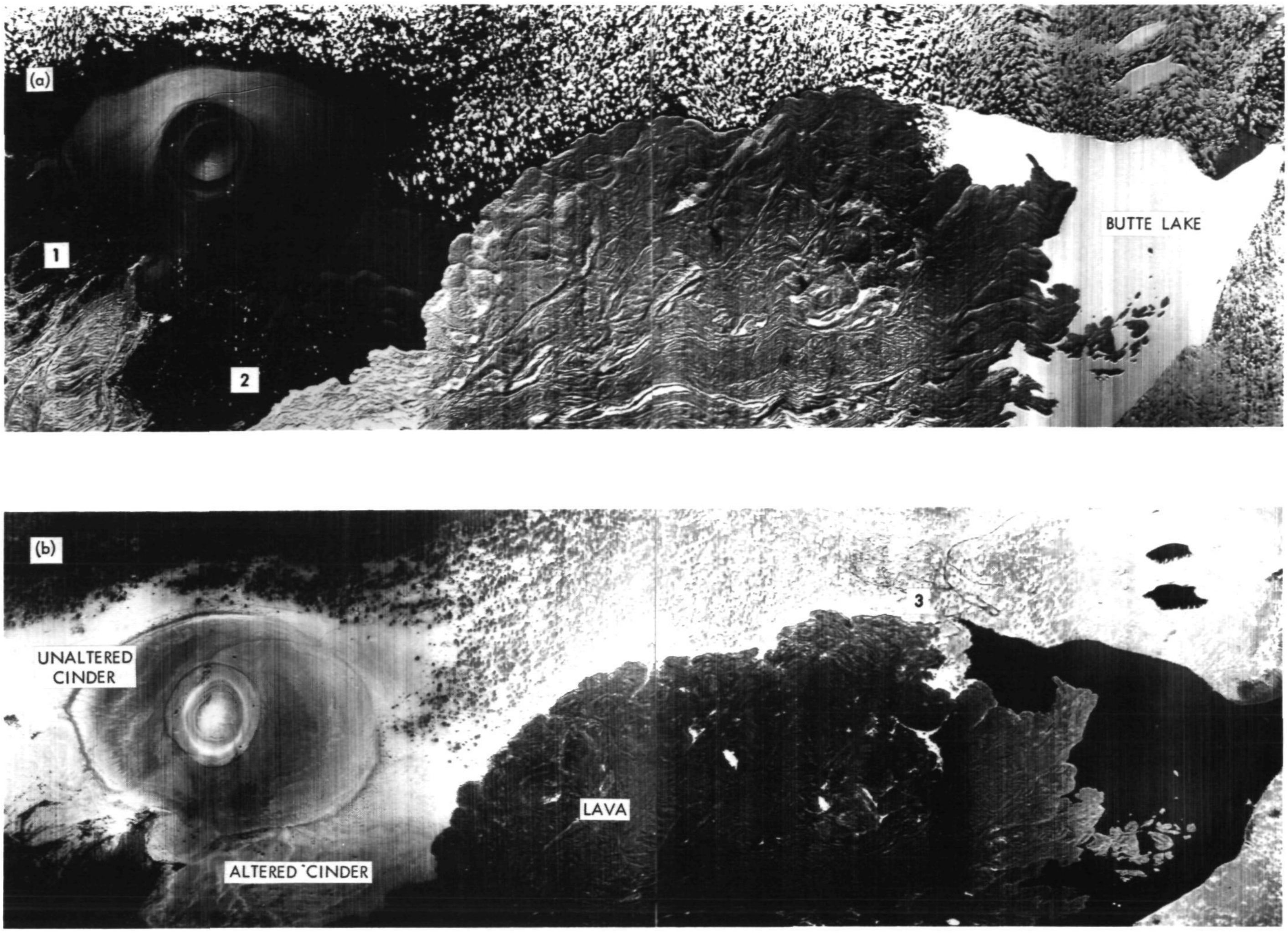

Fig. 9. Thermal IR imagery: (a) Midday[2], (b) Predawn

At the time the imagery was flown, there was an excellent thermal contrast between the ridges and valleys of the lava flows. This contrast enhanced the flow structures of the lava and stress patterns created at the time that the flow surface cooled. The day imagery shows a high amount of distortion, which may have been caused by air turbulence.

Where the cinder is known to overlie the lava, in the area of altered cinder, the day imagery shows anomalies (areas 1 and 2 of Fig. 9a). This thermal contrast is probably due to the degree of alteration of the cinder covering the lava flows.

Figure 9b is the predawn thermal imagery. There has been a complete thermal inversion, with the cinder now becoming the coldest and the water the warmest. The basalt remains warmer because of its ability to transfer stored subsurface energy to the surface. The compacted dirt roads in the campground (area 3 of Fig. 9b) are now visible and are warmer due to their higher thermal diffusivities. Larger particles on the sides and base of the cinder cone may be distinguished from fine cinder; the larger blocks being warmer due to their greater thermal capacity.

Several areas, which are topographic lows on the cinder fields, are colder due to settling of cold air. This phenomenon is readily visible at the depressed center of the cinder cone.

The diurnal radiometric temperature shown in Fig. 10 illustrates that the predawn imagery generated at approximately 0400 h was flown at the time of maximum contrast

---

[2] Dark areas indicate warmth.

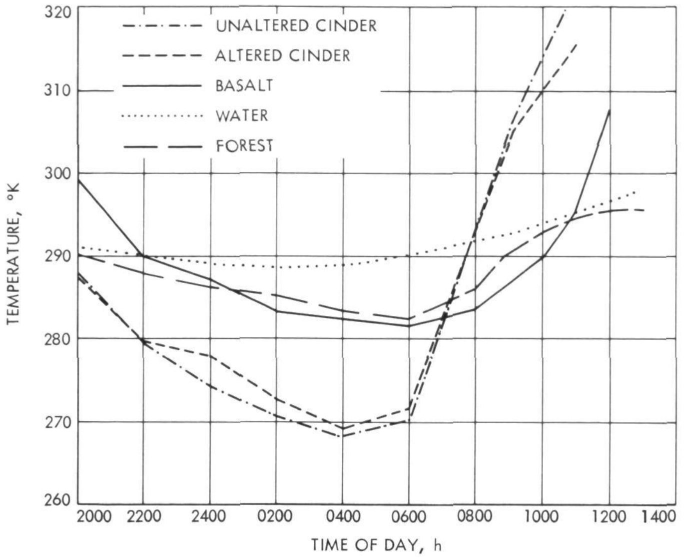

Fig. 10. Diurnal radiometric temperatures

between the principal units under study. If, however, one were trying to locate thermal anomalies such as hot springs, fumaroles, etc., the ideal time would be at 0700 h when all the principal units would be at equilibrium. This clearly demonstrates the advantage of prior field studies in selection of optimum flight times, if thermal properties are to be used in differentiating rock units for geological interpretation.

VI. Scatterometry

The scatterometer is an active radar system which records radar reflections along the flight path of the aircraft. Data on radar scattering at a variety of illuminating and receiving angles may be sampled on a single flight. Scatterometry data are normally presented as reflectance or sigma curves, which plot return against look angle for each integration cell along a flight line. The data in this report are presented as distance-versus-return (time) plots for each of a number of look angles.

The 13.3 GHz scatterometer, used at the Mt. Lassen test site, isolates individual resolution cells by combining a fan-beam antenna with sampling at preset doppler frequency shifts. The fan-beam antenna illuminates a swath of terrain about 3 deg in width from angles of 60 deg fore to 60 deg aft. The width of the resolution cell is, therefore, 3 deg. The angular measurements needed to define the remaining two edges of each resolution cell are obtained from sampling specific doppler frequencies in the returning echo. Each angle has its own doppler frequency as defined by:

$$f_{\mathrm{D}} = \frac{2v}{\lambda} \sin \theta$$

where f_{D} = doppler frequency

λ = wavelength

v = velocity

θ = look angle

Figure 11 shows the shape of the fan beam and the size of the resolution cells for the Mt. Lassen mission.

A. Roughness Determination

In order to differentiate the various surfaces at Mt. Lassen, the Rayleigh criterion of roughness can be applied to the resulting scatterometer data.

If ray a and ray b at grazing angle γ are coming in contact with a surface of irregularities of height h, as in Fig. 12, the path difference (Δr) is: $\Delta r = 2h \sin \gamma$, hence, the phase difference is

$$\Delta\phi = \frac{2\pi\Delta r}{\lambda} = \frac{4\pi h}{\lambda} \sin \gamma$$

At $\Delta\phi = \pi$ the rays come into phase opposition and cancel, the surface is considered rough, $\Delta\phi = 0$ smooth, and $\Delta\phi = \pi/2$ intermediate. By the Rayleigh criterion a surface is considered smooth for

$$h < \frac{\lambda}{8 \sin \gamma}$$

Using this criterion the dividing point between diffuse and specular surfaces can be seen in Table 8.

Table 8. Dividing point between diffuse and specular surfaces

Grazing angle, deg	Scatterometer angle, deg	Particle size h, cm
85	5	0.282
55	35	0.343
45	45	0.398
30	60	0.562

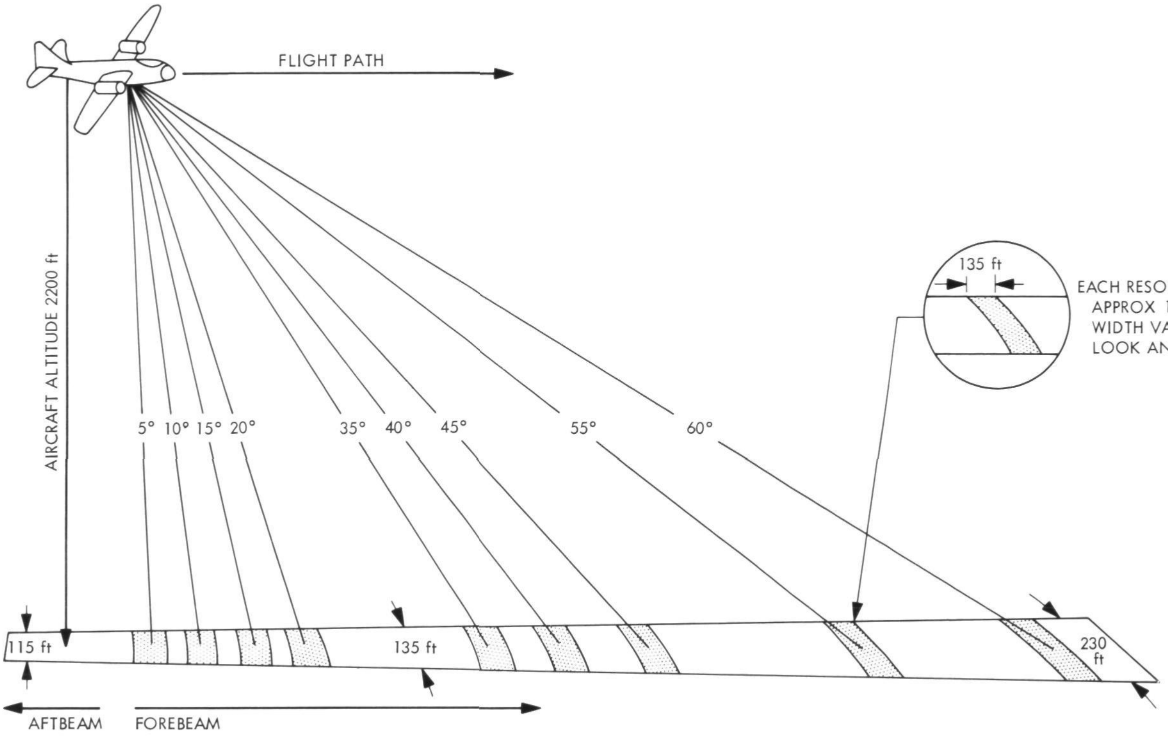

Fig. 11. Scatterometer fan-beam geometry

Since the lava blocks average 30 cm in diameter, they are considered diffuse surfaces regardless of grazing angle. The cinder is exactly at the dividing line between specular and diffuse, while the lake surface on the day of the overflight was specular at all angles. The forested areas, when the above criterion is applied, are extremely diffuse scatterers, but since vegetation has a greater absorptivity than either the cinder or basalt, it must be considered as a special case.

Figure 13 is a smoothed diagram of the forebeam scatterometer data over line 2. The idealized portion of the diagram indicates the probable return if all the surface had the same absorptivity.

B. Topographic Variations

Topographic variations on the scale of tens-of-feet can be observed on the Mt. Lassen scatterometer data. If a fixed transmission and reception point is considered, the Rayleigh criterion states: given two surfaces of equal roughness, the one with the more gentle hill-to-valley slopes should scatter less diffusely. The basalt flows, like the cinder, tend to form a rolling-hill topography. However, since the basalt is such a diffuse scatterer, the rolling-hill topography is masked on the data and is only noticeable on the more specular reflecting cinder fields. This diffuse masking of slope should be considered when interpreting radar data, such as fault locations on radar imagery. Figure 14 shows the theoretical scattering diagrams of the three principal surfaces (conifer forest excluded).

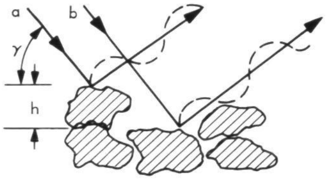

Fig. 12. Sketch of ray phases

Topographic variations are observable on the data. When points on the ground can be identified at several return angles, the time taken to traverse the distance between the points at varying look-angles may be used to determine slope. Slopes determined in this manner represent the average slope between any two identified points, if the aircraft is in level flight at a constant speed.

When terrain slopes toward the aircraft higher return-angle, forward-looking data are apparently lengthened. This is illustrated in Fig. 15. Where the terrain is level,

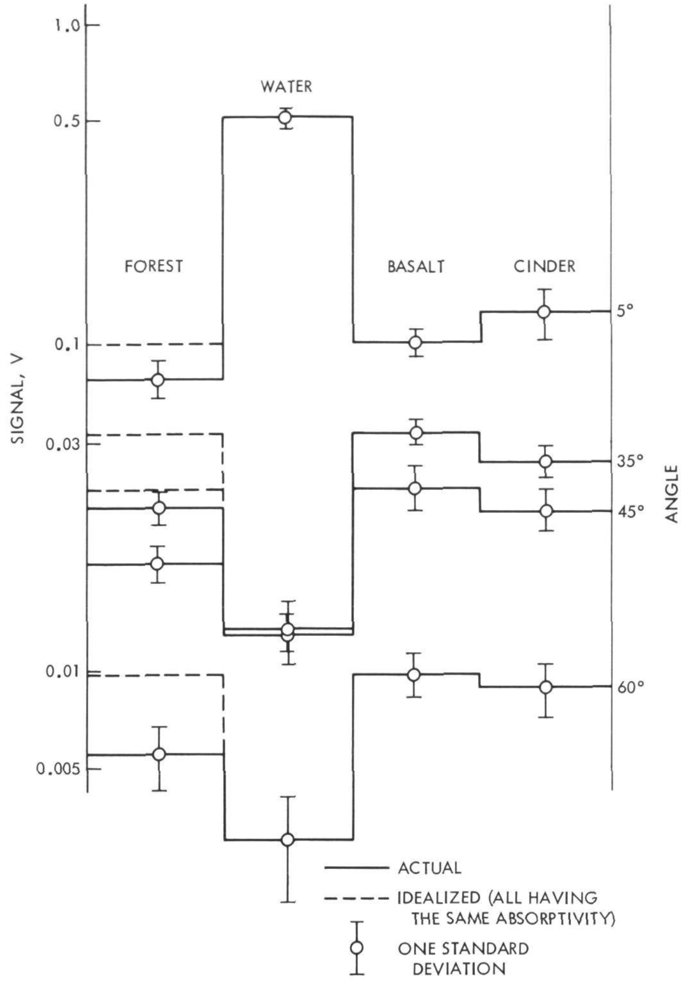

Fig. 13. Idealized scatterometer returns

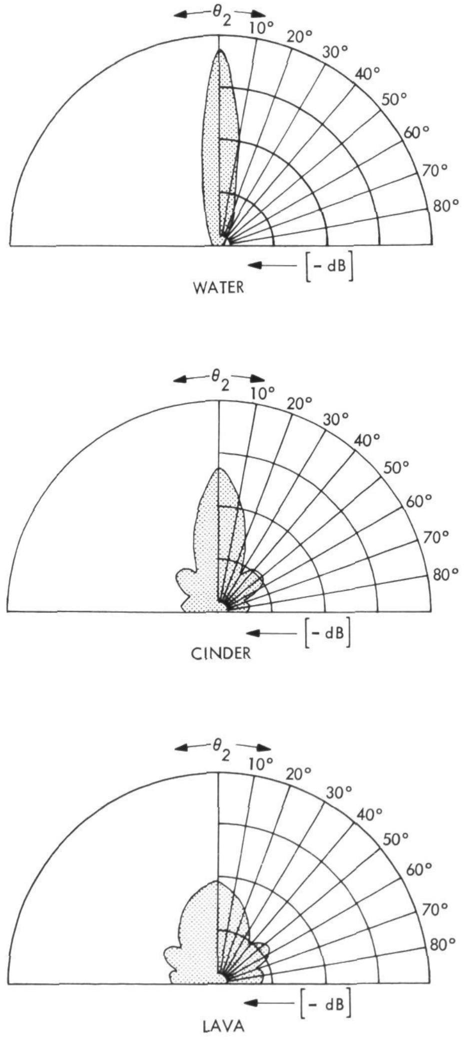

Fig. 14. Theoretical scattering diagrams of the three principal surfaces

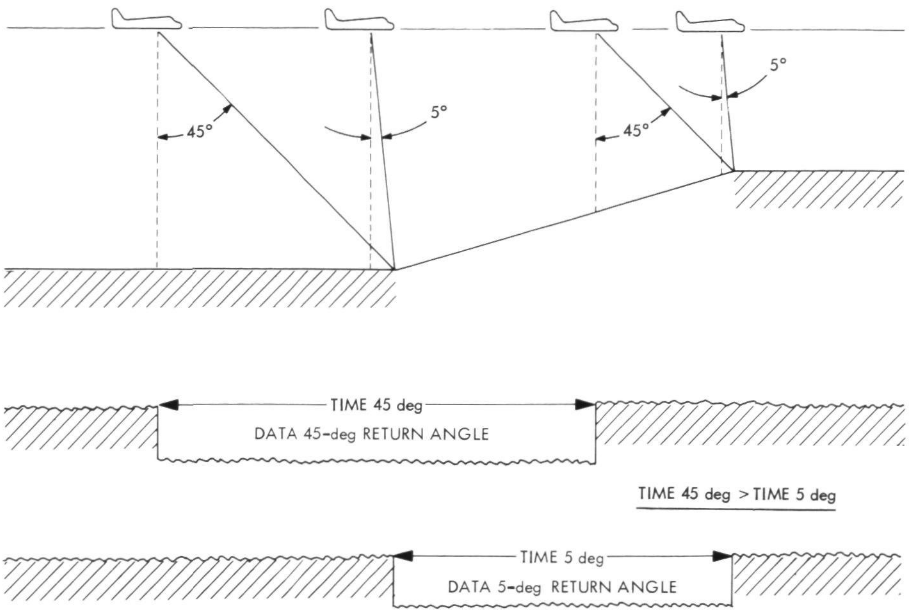

Fig. 15. Influence of topography on scatterometer delay times

the times between two points are equal at all look angles. When the land slopes away from the aircraft, the high return-angle data are apparently fore-shortened with respect to the low return-angle data.

The data shown in Fig. 16 have been sloped and scaled so that the west shore of Butte Lake and the first cinder-basalt contact are aligned. The reference plane to which the data are fit is, thus, slightly inclined. Advancement or retardation of data points, shown in Fig. 16, represent changes in slope relative to the average slope between the two alignment points. The altered cinder area is relatively lengthened at greater look-angles indicating an increase in slope in the direction of the oncoming aircraft. The basalt area to the southwest of the cinder is greatly fore-shortened at large look-angles, indicating a decrease in slope in the direction of the oncoming aircraft.

By producing time-versus-return plots such as in Fig. 16, from data received from flying over areas with significantly large homogeneous lithologic units, information on roughness characteristics and topography can be expected from the scatterometer over many geologic targets.

VII. Microwave Radiometry

A. Ground-Based Studies

To enhance the data obtained by the aircraft microwave radiometers and to better understand the factors affecting the microwave signature, ground-based studies were conducted in conjunction with and prior to the aircraft overflights. Table 9 lists the radiometer frequencies utilized during the investigations. The ground-based 9.3 GHz radiometer was supplied by the Jet Propulsion Laboratory (JPL). The remainder of the ground-based radiometers were provided by the Aerojet-General Corporation Remote Sensing Field Laboratory, under contract to JPL.

The two units operating at the Poison Lake cinder pit are shown in Fig. 17. With the exception of the 1.4 GHz channel, which had interference problems most of the time, the radiometers operated satisfactorily during the course of the studies.

Studies were conducted at four sites, Mono Lake, the ABC Block Company gravel pit in Reno, Nevada, the

Table 9. Microwave frequencies

Airborne, GHz	Ground-based, GHz
–	1.4
8.9	9.3
15.8	13.7
22.2	–
34.0	37.0

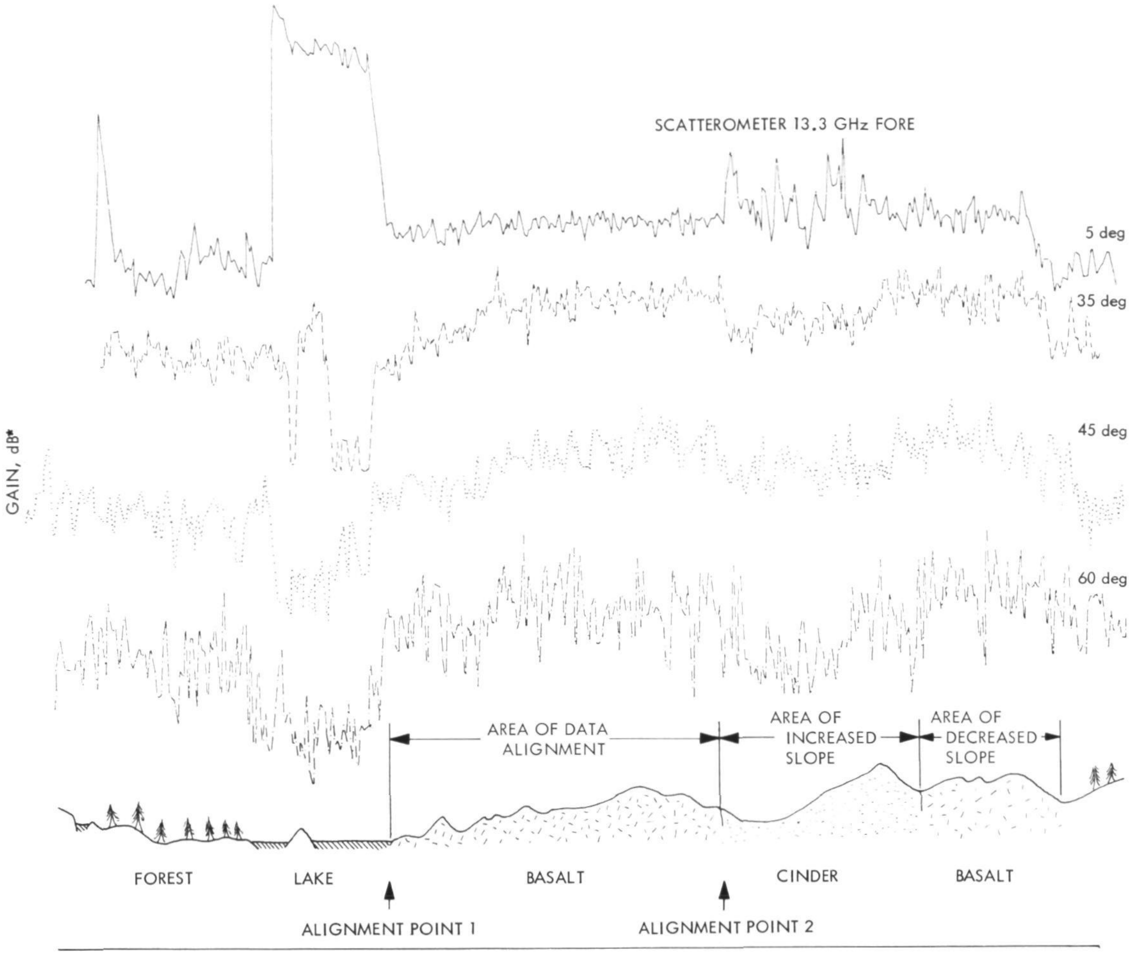

*dB GAIN LEVELS HAVE BEEN ADJUSTED FOR CLEARER ILLUSTRATION

Fig. 16. Time delay shifts in scatterometer data due to topography

Fig. 17. JPL and Aerojet-General Corporation microwave vans at Poison Lake cinder pit

Poison Lake cinder pit, and the basalt flows at the Mt. Lassen Test Site. Their purpose was to:

(1) Obtain microwave data for calibration of the aircraft microwave radiometers, thus correcting for effects of radome and antenna losses.

(2) Determine microwave penetration depth.

(3) Examine effects of particle size on microwave emission.

A chronology of the microwave radiometric field measurements is shown in Table 10.

B. Microwave Penetration Depth

The microwave penetration depth α is defined as the thickness of material required to attenuate a microwave signal passing through it to $1/e$ of its original value.

Table 10. Chronology of microwave radiometer field measurements

Date, July 1968	Site	Description	Time of day, h		Tests performed
			Start	Stop	
9	Mono 1	Pumice flat	1030	1350	Fixed angle traverse
10	Mono 1	Pumice flat	1000	1100	Penetration depth, scans
	Mono 2	Lake sand	1300	1630	Penetration depth, scans
11	Reno	Assorted gravel	1100	1605	Penetration depth, limited scans
12	Reno	Assorted gravel	0950	1450	Penetration depth, limited scans
15	Lassen	Poison Lake cinder pit	1129	2400	Penetration depth, diurnal run (scans)
16	Lassen	Poison Lake cinder pit	0000	1410	Diurnal run (scans)
18	Lassen	Butte Lake H_2O	0950	1025	9.3 GHz only
18	Lassen	Butte Lake basalt	1125	1505	Scans during overflight No. 4
19	Lassen	Butte Lake basalt	0230	0440	Scans during overflight No. 5

Determination of α gives a quantitative measure of the depth to which microwave radiometers can "see." The α may be measured in the field by two methods; by viewing a reflecting plate covered with varying thicknesses of material, and by studying the diurnal variations in microwave emission. For particulate matter, the buried plate technique offers advantages in speed, accuracy, and uniformity of samples. The diurnal method offers the potential of measuring α for non-particulate matter and in cases where *in situ* measurements are preferable.

1. Buried-plate technique. The buried-plate technique and results obtained during this experiment are discussed by Conel (Ref. 2). For completeness, his results are summarized herein.

In this technique, a metallic plate is covered by varying thicknesses of a material, uniform in water content and temperature. Brightness temperature is plotted as a function of material thickness on semilog graph paper. The α is determined from the slope of the line. The results of these measurements are summarized in Table 11.

These results show that α, as expected, is a function of frequency. For reasonably dry sand and cinder, α is on the order of several wavelengths at all of the frequencies. Figure 18 shows the relationship for dry and wet sand. The presence of water greatly decreases penetration depth.

The uncertainties in plate measurements arise in obtaining uniform composition, thickness, temperature and moisture. Antenna temperatures increasing in a uniform asymptotic manner with plate depth provide a check on the validity of a particular measurement.

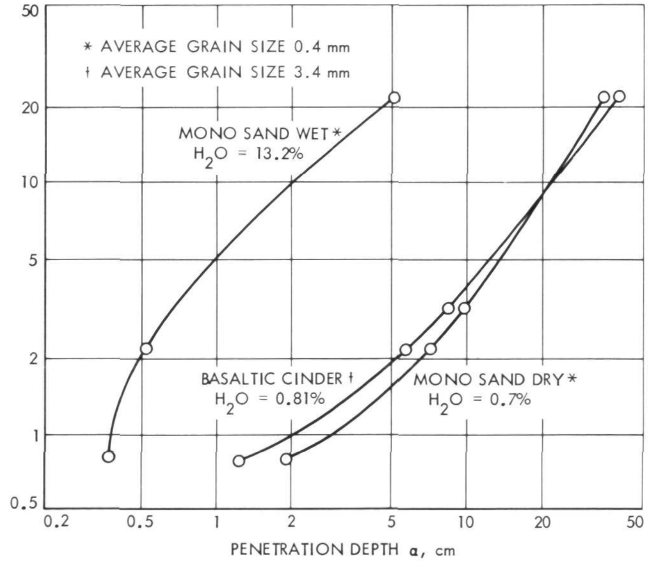

Fig. 18. Penetration depth vs wavelength

2. *Diurnal measurements*

a. Cinder. Data were collected over a 24-h period at the Poison Lake cinder pit in order to obtain calibration data for the aircraft overflight and to obtain an estimate of the penetration depth from *in situ* measurements. Graphs of the physical temperatures at depths of ½ in., 2 in., 4 in., 8 in. and 3 ft and the radiometric temperatures for the 24-h period are shown in Figs. 19, 20a, and 20b, respectively.

Table 11. Summary of penetration depth measurements

Site	Material	Composition	Particle size, mm		Surface	Water, %	Density	Temp, °K	Penetration depth α, cm			
			Mean	σ					1.4 GHz Radiom	9.3 GHz Radiom	13.7 GHz Radiom	37.0 GHz Radiom
Mono 1	Pumice sand	Basaltic	1.43	2.20	Rough	0.27	1.19	317	–	–	8.2	–
Mono 1a	Pumice sand	Basaltic	1.20	3.70	Rough	1.74	1.15	318	–	–	–	1.8
Mono 2	Pumice sand	Basaltic	0.42	0.33	Rough	0.67	1.14	318	34.4	9.7	7.2	1.9
Mono 2, wet	Pumice sand	Basaltic	0.46	0.24	Rough	13.23	1.14	318	5.1	–	0.52	0.37
Reno 1	Aggregate	Pumice	12.6	2.53	Rough	0.11	1.17	316	–	5.5	2.6	1.1
Reno 2, wet	Pea gravel	Pumice	5.40	1.68	Smooth	6.53	1.50	310	–	0.65	–	–
Reno 2	Pea gravel	Pumice	5.40	1.68	Smooth	0.92	1.50	307	–	6.8	4.0	3.3
Reno 2, SG			5.40	1.68		0.84	1.38	308	–	–	–	–
Reno 4			11.20	2.53		0.67	1.38	316	–	–	–	–
Reno 3			–	–		–	0.98	–	–	–	–	–
Mt. Lassen	Cinder	Basaltic	3.40	2.50	Rough	0.81	1.10	323	40.3	8.6	5.8	1.25

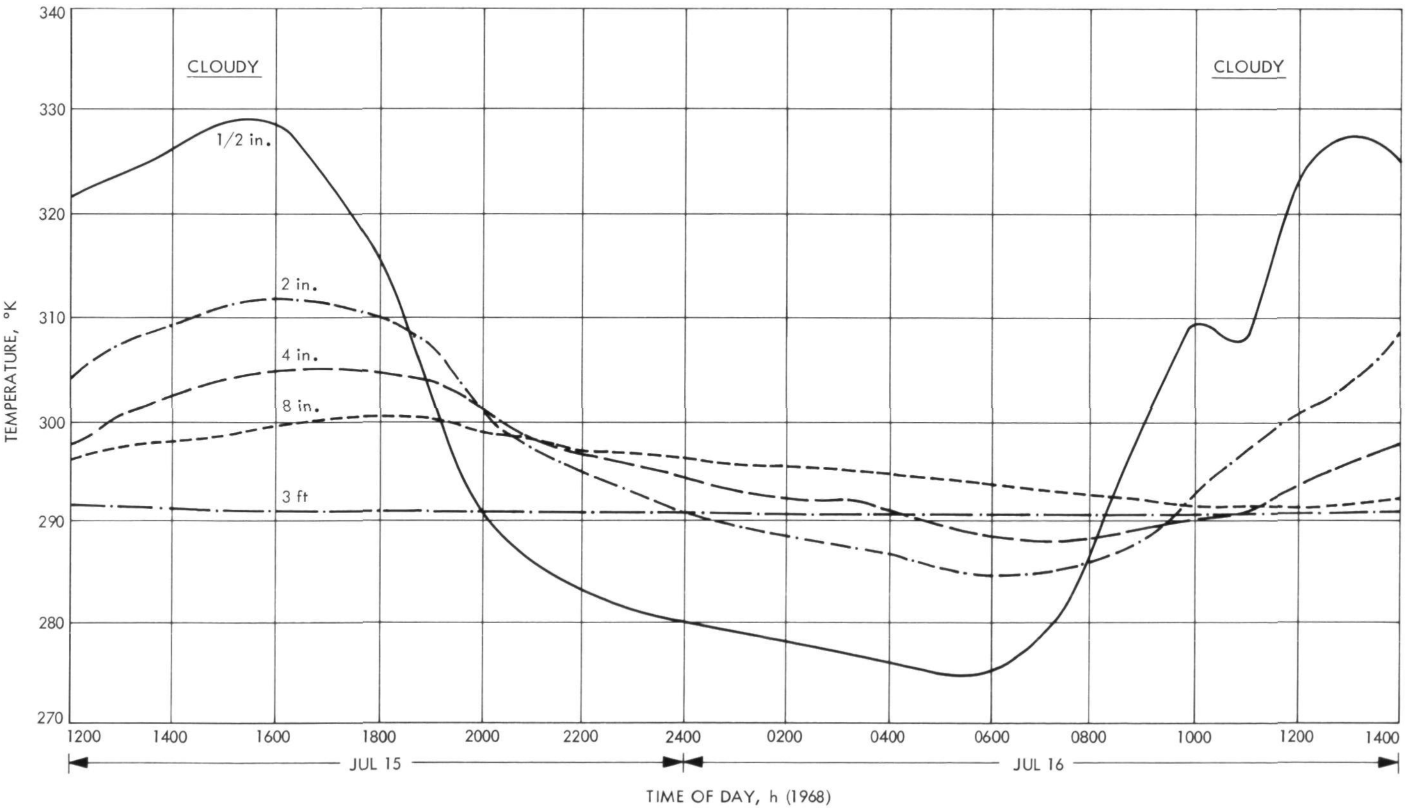

Fig. 19. Thermistor probe temperatures, Poison Lake cinder pit

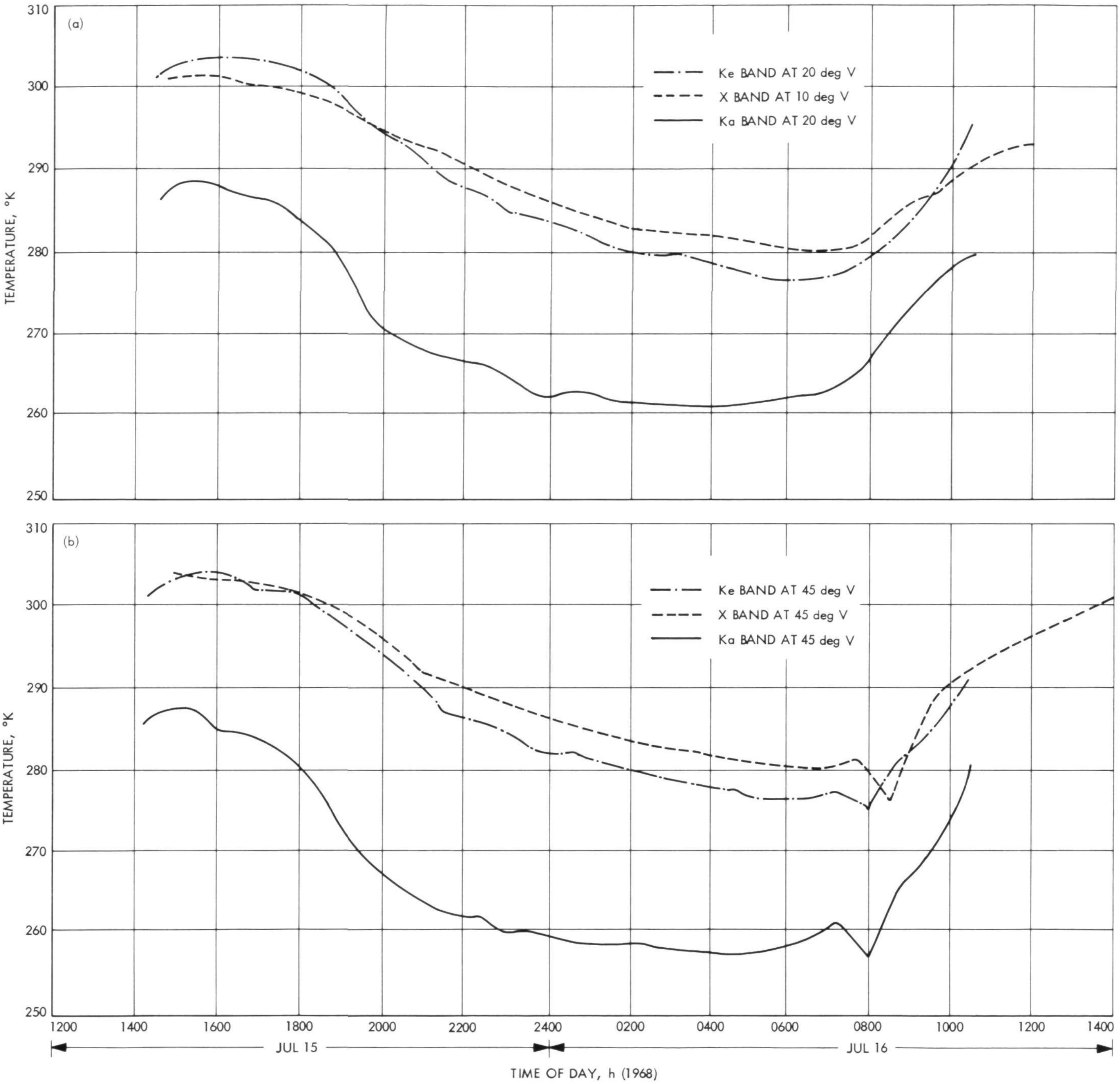

Fig. 20. Microwave temperatures, Poison Lake cinder pit

Figure 19 shows that changes in temperatures with increasing depth are twofold; the magnitude of the fluctuations decreases and the location of the maximum and minimum occur later in time. Table 12 lists the magnitude of the fluctuations and the time of the maximum and minimum. Table 12 also lists the magnitude of the temperature variations and maximum and minimum positions for the diurnal radiometer responses. The normalized microwave temperature difference δT_n, is the magnitude of the difference divided by the emissivity measured at 2000 h when the ground was close to being equithermal.

Table 12 shows some interesting comparisons. The temperature deviations of the 13.7 GHz channel compare with those of the 2-in. probe. The 9.3 GHz channel lies

Table 12. Comparison of diurnal extremes

Thermometric				Radiometric			
Depth, in.	δT_{peak}, °K	t_{max}, h	t_{min}, h	λ, cm	δT_{n}, °K	t_{max}, h	t_{min}, h
½	54	1530	0600	0.8	31.0	1530	0430
2	27	1600	0600	2.2	27.5	1700	0600
4	17	1700	0730	3.2	22.0	1500	0640
8	9	1830	1000	21.0	–	–	–

midway between the 2-in. and 4-in. probe or approximately to the readings of that would be obtained at 3 in. The δT_{n} for 37.0 GHz is greater than that for 13.7 GHz, but not nearly so large as one would expect considering the difference between δT_{peak} for the ½-in. and 2-in. depth placement of the probes. The times of the maximums and minimums tend to increase with increasing wavelength. However, the times of occurrence and the 9.3 GHz maximum are anomalous.

b. Basalt. During the overflights, data were taken over an area of basalt which was accessible to the instrument vans. The basalt fields were hills of large blocky basalt. Since the ground based radiometer views only a small area, in some cases looking at individual rocks, these measurements are only indicative of the results one may expect from an aircraft radiometer which views large areas. Thermistor and radiometer temperature data for the basalt are shown in Figs. 21, 22a, and 22b.

c. Roughness effects. The effect of roughness on microwave emission is a little understood phenomenon. Although several models exist, a real surface is often a composite of model surfaces. The expected responses from three model surfaces are represented in Fig. 23.

The characteristic microwave response of a specular surface, as a function of viewing angle and polarization, is shown in Fig. 23a. As the surface becomes less specular (more diffuse) the vertical and horizontal polarization responses tend to come together in some fashion. The predictions of two scattering models are shown in Fig. 23b. In the Lambert Scattering Model, they merge, but do not fall off with increasing angle. In the Grass Model, they merge and fall off with increasing angle. If these three models were each reduced to a point in plane at which the axes were the difference between V-H at angle θ_1, and the difference between the vertical polarization data

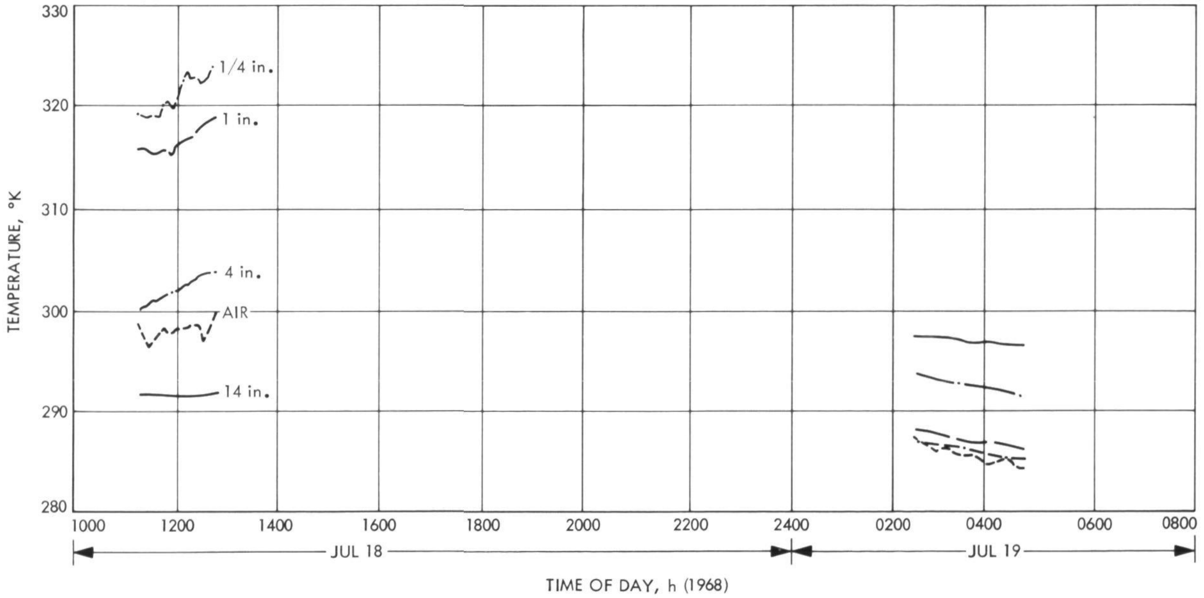

Fig. 21. Thermistor probe temperatures, Butte Lake basalt

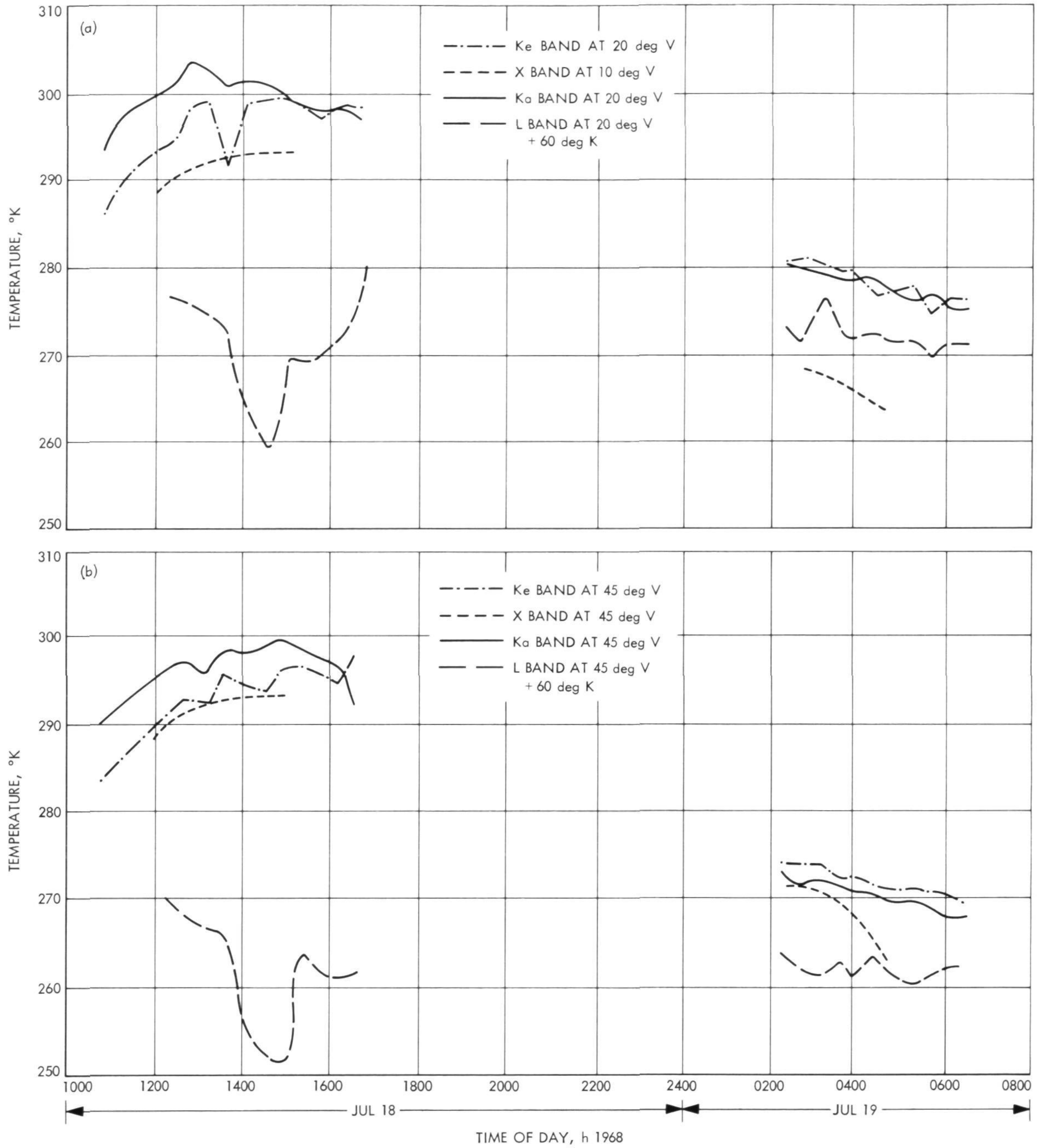

Fig. 22. Microwave temperatures, Butte Lake basalt

at angles θ_1 and θ_2, they would fall into three distinct domains as shown in Fig. 23c.

Phase diagrams in this format with $\theta_1 = 45$ deg and $\theta_2 = 10$ deg are shown in Fig. 24 for the diurnal data from the basalt and cinder. Since the same basalt areas were not viewed by both vans, the 9.3 GHz basalt data were not included in this diagram. The most interesting feature of this graph is that the points fall into a tight scatter diagram, regardless of time of day, and show a definite trend toward a specular response with increasing wavelength. It is also interesting to note that basalt and cinder look equally rough at 37.0 GHz and fall in the domain of the Grass Scattering Model.

Consider now the expected behavior of the points within the scatter diagram, as a function of the time of

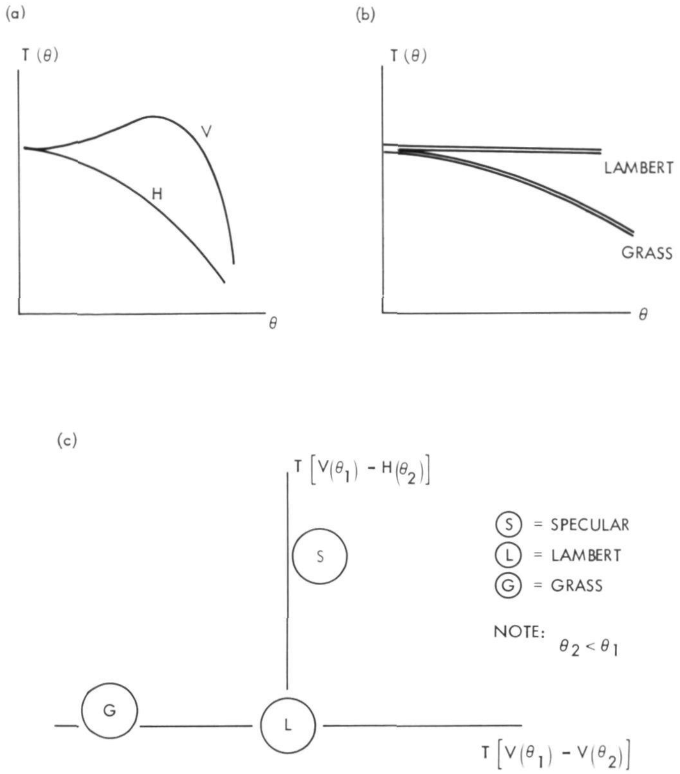

Fig. 23. Sketches of responses from model surfaces: (a) Specular model, (b) Scattering models, (c) Phase diagram

day. At larger incidence angles, it is expected that the effective depth of penetration will be less than at angles closer to the vertical. Hence, during the day when the surface is heating, one would expect the 45 deg component to increase faster than the 10 deg component. Hence, the difference, T(45 deg) − T(10 deg), would increase. Conversely, at night one would expect the difference to decrease. Little change is expected in the V-H component. The expected behavior is shown in Fig. 25. Figure 24 segregates the afternoon points from those taken at other times of the day. For the cinder, the response behaves as expected from the above consideration. However, the basalt behaves in the opposite manner. It is evident that understanding the motion of the point, as a function of time of day, could lead to a shrinking of the scatter diagram.

Figure 26 is a phase diagram for sand and three forms of gravel. In the 9.3 GHz and the 13.5 GHz channels there is a definite distinction among the sand, pea-gravel and larger gravels. The 13.5 GHz channel usually appears less specular than the 9.3 GHz channel, as expected. The

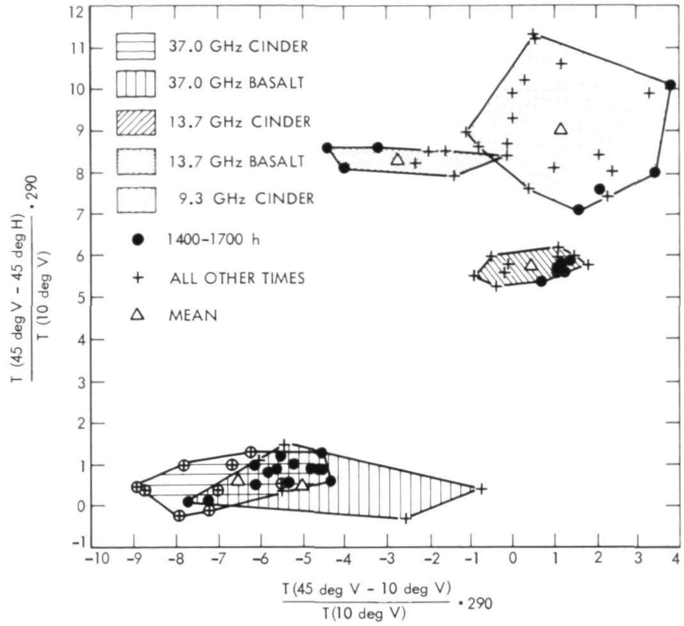

Fig. 24. Roughness phase diagram for cinder and basalt

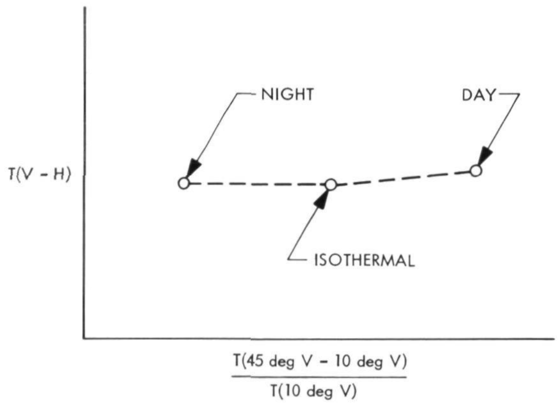

Fig. 25. Expected behavior of points within a scatter diagram

exception occurs over the Mono sand. This may be due to the significantly larger beamwidth at 9.3 GHz or an error in the angular position of the 9.3 GHz radiometer. Figure 26 also shows that everything looks rough at 37.0 GHz.

Examination of the varied materials shown in Fig. 26 on a diurnal basis may well show that points fall into tight domains similar to those shown in Fig. 24. Hence, this technique offers the potential of a quick graphical technique for determining the roughness characteristics of an area independent of time of day or year.

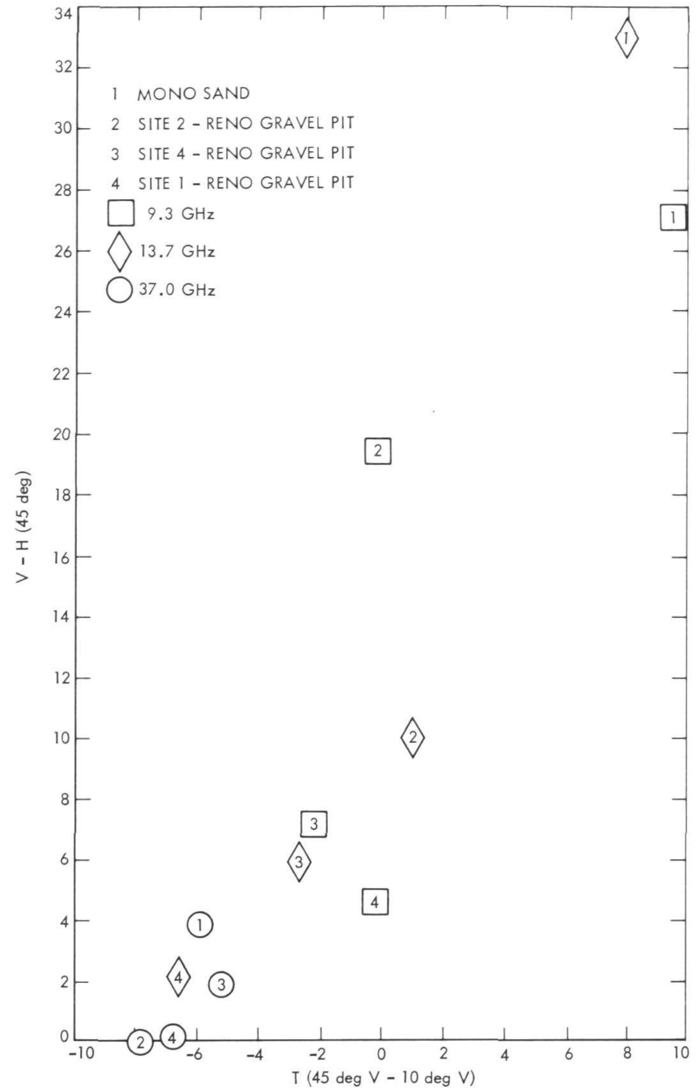

Fig. 26. Roughness phase diagram for gravel and sand

C. Airborne Microwave Radiometry

1. Calibration of aircraft data. Data over water and cinder were used as a two-point calibration for the aircraft microwave radiometers. As noted in Table 9 the frequencies on the ground were different than those used in the aircraft. The ground-based data at 9.3 GHz, 13.5 GHz and 37.0 GHz were used directly to calibrate the 8.9 GHz, 15.8 GHz, and 34.0 GHz airborne channels respectively. In the absence of ground-based data at 22.2 GHz, the average of the 13.7 GHz and 37.0 GHz values were used for the 22.2 GHz airborne channel.

The difference in emission between water and cinder provides a large differential for determination of radiometer gains. Due to logistic and experimental time constraints, ground-based measurements of the lakes were not obtained. Hence, the theoretical values of brightness temperature for water listed in Table 13 were used for calibration of the aircraft data.

Table 13. Aircraft calibration data, water

Look angle, deg	Polarization	Brightness temp/channel, °K			
		8.9 GHz	15.8 GHz	22.2 GHz	34.0 GHz
10	H	110	116	140	139
10	V	113	118	142	139
30	H	100	106	135	127
30	V	125	131	154	153
45	H	86	92	125	114
45	V	144	150	176	175

Since the cinder at the test site was inaccessible, data were from the diurnal runs at the Poison Lake cinder pit and were used for calibration of the aircraft radiometers. Values of microwave temperature used for calibration were selected by time-of-day rather than matching temperature profiles since temperature is very critical to placement of the temperature probes. The values used for calibration of the aircraft data are listed in Table 14. Day values for the 13.7 GHz and 37.0 GHz channels were determined by linear interpolation of the 10:00 a.m. and 2:00 p.m. data.

2. Aircraft data. The microwave radiometers duplicated the results of the 1967 mission (Ref. 1). However, the added measurements of diurnal temperature variations and seismic profile data permit a more meaningful interpretation of the results. An example of the day and night multifrequency microwave responses over line-two are shown in Figs. 27a and 27b. The 8.9 GHz and 34.0 GHz responses at night show a definite delineation of the basalt and cinder. The 34.0 GHz day response also shows this delineation.

The dominant parameters affecting the response are the material thermal properties and emissivity. Consider the expected microwave responses in light of the thermometric data of the basalt and cinder shown in Figs. 19 and 21. During the day flight (1100 h) the temperatures near the surface are about the same. Hence, one would expect, all other factors being equal, that the 34.0 GHz channel with its small penetration depth, would show a uniform response. However, it shows the cinder to be cooler. Thus, at 34.0 GHz, the emissivity

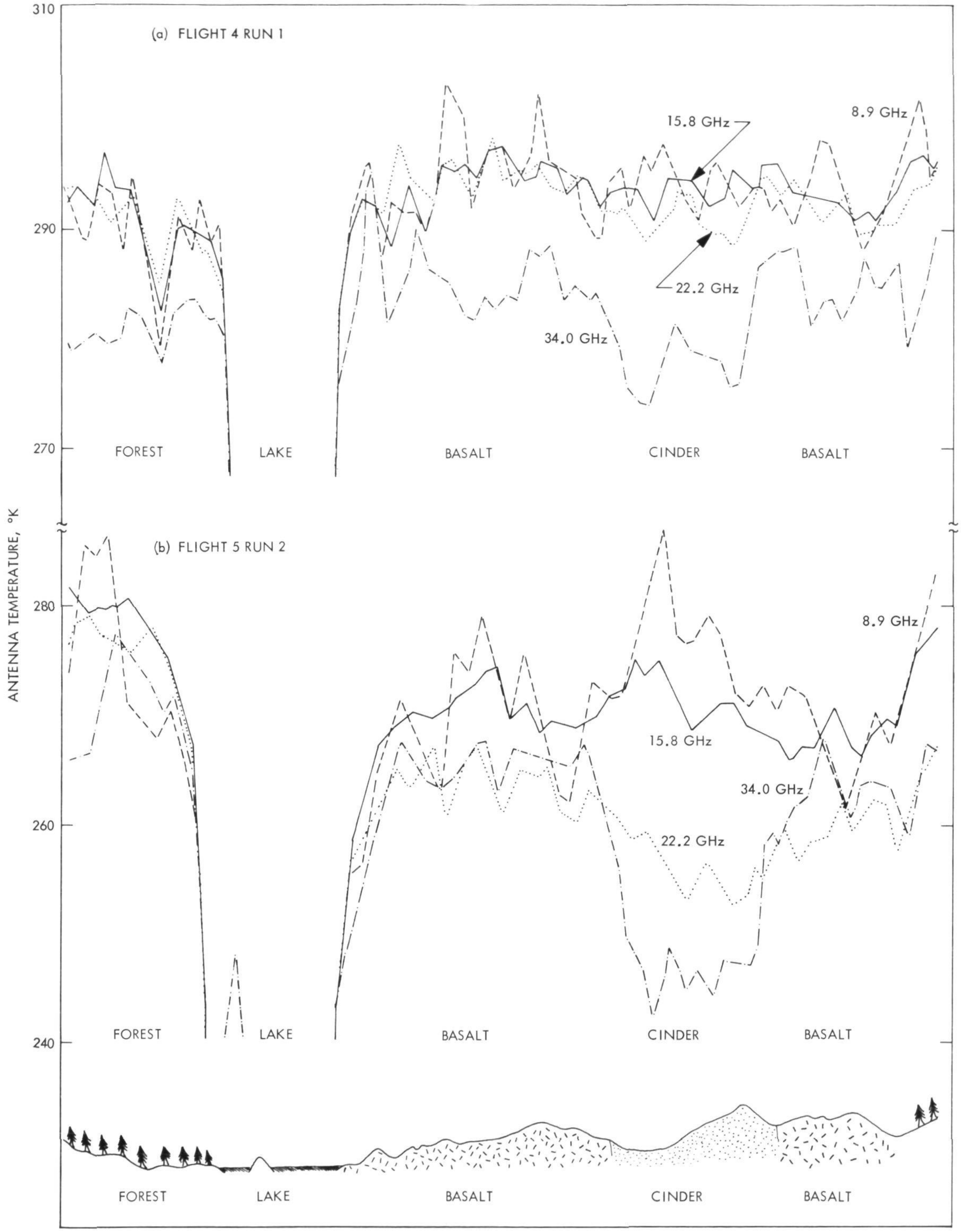

Fig. 27. Aircraft microwave data: (a) Midday, (b) Predawn

Table 14. Aircraft calibration data, cinder

Look angle, deg	Polar-ization	Brightness temp/channel, °K							
		8.9 GHz		15.8 GHz		22.2 GHz		34.0 GHz	
		Day	Night	Day	Night	Day	Night	Day	Night
10	H	293.2	282.5	293.4	280.2	288.8	271.5	284.3	262.8
10	V	294.3	282.4	293.4	280.0	288.8	271.2	284.2	262.4
30	H	291.6	279.5	293.3	277.9	287.5	269.3	281.8	260.7
30	V	296.2	283.2	295.4	280.2	288.8	270.3	282.2	260.5
45	H	280.8	273.5	288.8	274.3	283.5	265.3	278.1	256.4
45	V	297.6	283.7	294.0	279.4	286.4	267.8	278.8	256.3

of the cinder is less than that of the basalt. Now consider the 8.9 GHz channel, which has a penetration depth α of 3.4 in. in cinder. The α was not measured for basalt and the authors are not aware of a theory relating penetration depth to density ρ in the microwave region. For want of a better relation, assume that $\alpha \propto e^{-\rho}$, a valid equation in the x-ray portion of the spectrum.

Then

$$\alpha_{\text{lava}} = \alpha_{\text{cinder}}\, e\left(\frac{\rho_{\text{lava}}}{\rho_{\text{cinder}}}\right) = \alpha_{\text{cinder}}\, e^{-2.35}$$

using the values of density contained in Section II-C above. The penetration depth of basalt is estimated to be 0.34 in.

From the ¼-in. probe and thermistor probe data, thermal considerations indicate that the 8.9-GHz response during the day should show the cinder to be cooler than the basalt (it shows no change) and during the night should show a little change (it shows the cinder to be warmer). These results are summarized figuratively in Fig. 28. The results at 8.9 GHz are explained by a higher emissivity for cinder than basalt, which compensated for the temperature differences during the day. Hence, it appears that the emissivity of cinder is less than that of basalt at 34.0 GHz and greater than that of basalt at 8.9 GHz.

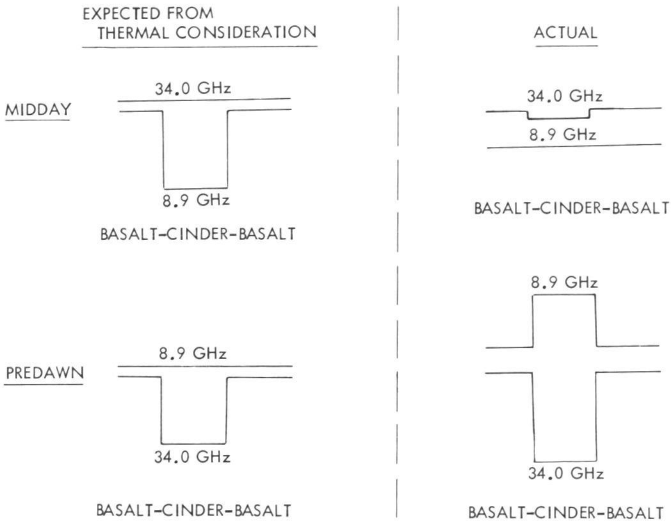

Fig. 28. Idealized microwave radiometer responses

VIII. Summary

A summary of the data received from the overflights is shown in Fig. 29 which shows the IR imagery, microwave radiometer day-night responses, color IR photography and radar scatterometer plotted on the same distance scale. In addition are an elevation profile of the flight line determined from existing base maps, a geologic map determined from aircraft data and ground studies, and vegetation density plots determined from color IR and black and white photography.

In Sections IV–VII above, the individual sensor outputs were examined in light of terrametric studies. Table 15 shows the parameters that can be determined with aircraft data only and the extent to which the aircraft data can be enhanced with terrametrics.

Terrametrics are considered to fall into three classifications; non-variant, variant, and advanced research. Non-variant parameters are nonchanging and understood.

Fig. 29. Overflight data summary

Page Intentionally Left Blank

Table 15. Relation of remote sensing data to terrametric information

Sensor	Aircraft data[a] (gross features)	Data interpretation with ground truth				Data interpretation with future research	
		Non-variant		Variant		Remarks, future research	
		Ground parameter	Sensor information	Ground parameter	Sensor information	Ground-based research	Sensor information
B&W Photo	1. Topographic variations 2. Geomorphic features 3. Plot aircraft track 4. Quantitative mapping of some geologic unit 5. Surface structural lithologic units 6. Some texture features	1. Survey (geodetics) elevations and locations (set flight altitudes) 2. Geologic reconnaissance	1a. Topographic mapping 1b. Quantitative stratigraphy 1c. Engineering geology 2a. Structural geologic maps 2b. Detailed mapping of geologic units			1. To determine the correct time and sun angle to enhance shadowing effects 3. Albedo measurements (i.e., optimum film and filter combinations)	1. Low sun-angle photography to accentuate geologic structures and land forms. 2. Use of high-speed film for determining the aircraft track during night flights 3. Differentiation of geologic parameters such as composition rock types and supporting vegetation using multispectral photography
Color Photo	1. All of the above 2. Lithologic variations 3. Contacts 4. Changes in vegetation 5. Major alteration	1. Albedo measurements (i.e., optimum filter combination) 2. Moisture studies	1a. Chemical variations/gross 1b. Differentiate units in alteration studies 1c. Differentiate vegetation 2. Weathering studies				
Color IR Photo	1. Vegetation a. Vigor b. Seasonal changes 2. Alteration (Particularly Fe^{+++})			1. Determine which vegetation is a function of which geologic unit (set filter combination) 2. Soil moisture 3. Vegetation survey	1. Differentiate geology as a function of vegetation 2. Gross/surface moisture 3. Map selected vegetation types		

[a] Data interpretation without ground truth.

Table 15 (contd)

Sensor	Aircraft data[a] (gross features)	Data interpretation with ground truth				Data interpretation with future research	
		Non-variant		Variant		Remarks, future research	
		Ground parameter	Sensor information	Ground parameter	Sensor information	Ground-based research	Sensor information
IR 8–14μ Imagery (Day/Night)	1. Relative surface thermal change 2. Thermal anomalies 3. Some geologic boundaries 4. Identify certain geomorphic features	1. Radiometric temperature 2. Albedo selected thermal diffusivities 3. Particle size sampling	1. Radiometric temperature map 2. Relative diffusivity (relative density and porosity) 3. Particle size variation map	1. Solar flux (optimum flight time) 2. Meteorological data 3. Moisture sampling	1. Semi quantitative thermal diffusivity 3. Surface moisture content	1. Study the IR signatures as a function of albedo, emissivity, thermal parameters and water content	1. To differentiate geologic units as a function of contained water (i.e., porosity permeability) before and after wet cycles
Multi Frequency Microwave (Day/Night)	1. Relative microwave surface and subsurface temperatures 2. Some geologic boundaries 3. Land—water boundaries 4. Thermal anomalies	1. Density and particle size	1. Map changes in density and porosity	1. Moisture sampling 2. Temperature as function of depth	1. Relative moisture content 2a. Microwave emissivity 2b. Microwave penetration depth	1. Emissivity dependence on water content 2. Roughness phase plot as a roughness classifier 3. Diurnal studies 4. Emissivity dependence on density	1. Determine water content as a function of depth 2. Determine gross roughness characteristics 3. Determine ratio of thermal diffusity to penetration depth 4. Determine density from radiometer
Radar	1. Topographic variations 2. Particle size variations 3. Geomorphic features	1. Particle size studies	1. Map relative change surface texture				

They need to be determined only once and they are, e.g.:

(1) Topography, roughness, and grain size.

(2) Density and porosity.

(3) Mineralogy and chemistry.

(4) Albedo and thermal diffusivity.

(5) Dry dielectric constant and emissivity.

The variant parameters are, e.g.:

(1) Meteorology

(2) Temperature.

(3) Soil moisture.

(4) Solar energy flux.

(5) Vegetation distribution and vigor.

These variant parameters are also understood, but, they change and must be determined at the time of the overflight. The advanced research parameters are non-variant and not understood. Understanding these parameters could lead to increased remote sensing capabilities. For example, if the effect of water content on microwave emissivity were understood, it may be possible to determine soil moisture as a function of depth with a multifrequency microwave radiometer.

Each of the three classes of terrametric parameters has two columns in Table 15, ground parameter and sensor information. The sensor information column lists the increased information obtained from the sensor, due to knowledge of the adjacent ground parameter.

It is evident from this table that there is some overlap in measured parameters. The object is to determine the tradeoffs in speed, cost, and accuracy of the different techniques. It is also evident that certain sensors can supply data required by other sensors. The ultimate goal of this study effort is to use the output of one sensor to reduce or eliminate the terrametrics required for interpretation of another sensor. An example of one potential multisensor application is shown in Fig. 30. Here photography is used to determine albedo, thermal IR to determine thermal diffusivity, which in turn permits calculation of microwave emissivity, and all with a minimum of ground measurements.

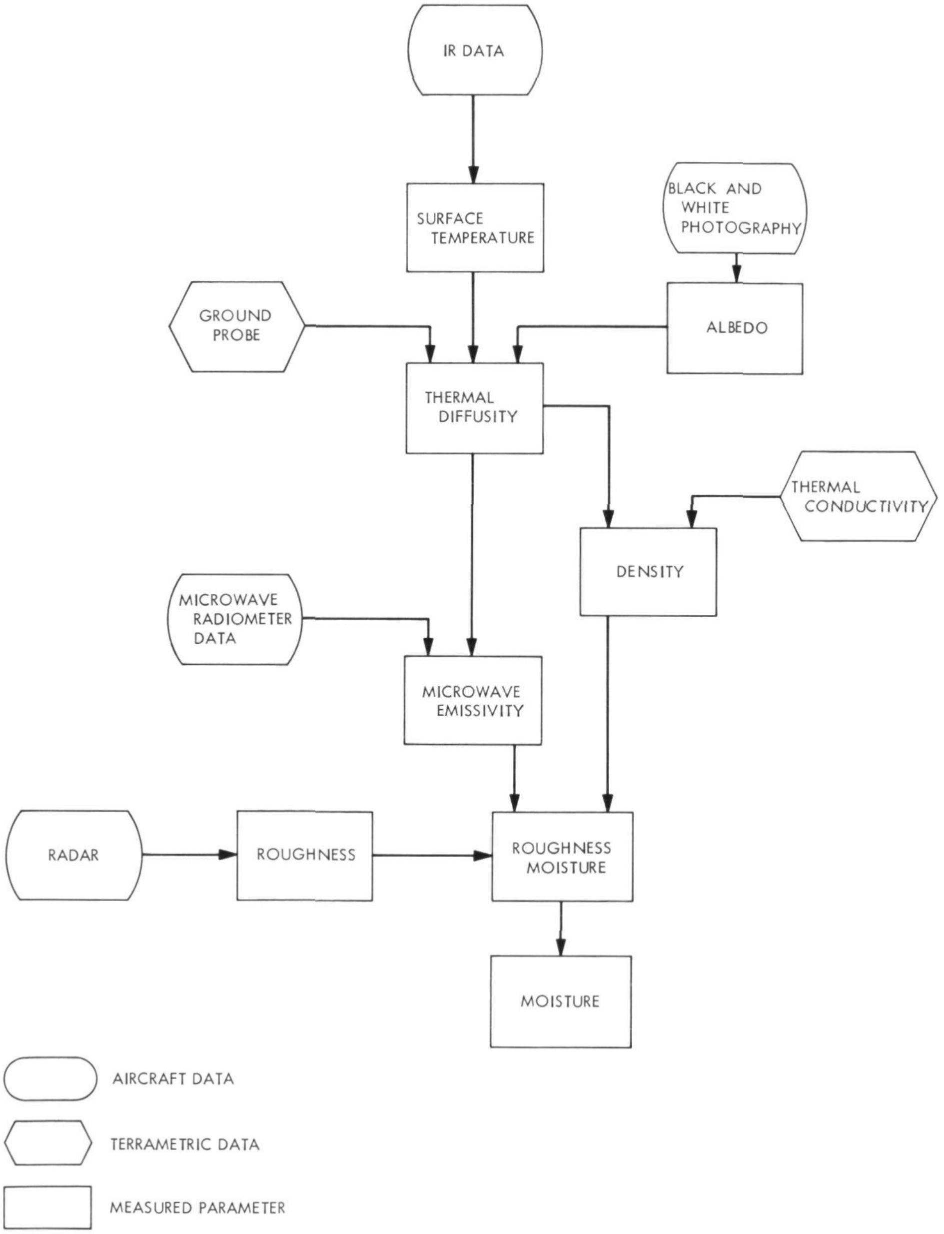

Fig. 30. Potential application of multispectral remote sensing

IX. Conclusions and Recommendations

It is concluded that each of the remote sensing systems studied have certain unique applications, but none of the systems, except photography, can be used effectively in geology by itself at this time. It is a further conclusion that none of the systems, including photography, can be used to its fullest advantage without some ground-based data.

While the aim of the airborne sensors is to cover large areas in a short period of time and eliminate as much time-consuming ground work as possible, it is equally important that costly aircraft data be well documented by ground-based measurements. During these early interpretative stages of remote sensing, ground data collection consumes much more effort than either aircraft operations or reconnaissance geology of a test site in the classical manner. However, as proficiency at interpretation and ground data collection become more sophisticated, with modest increases in ground calibration effort, vast areas of terrain may be sensed with confidence.

A. Photography

Metric photographs were flown, primarily to establish ground track and to quantify the vegetation. The particular film-filter combination used on the color IR photographs differentiated the various colors of cinder very well, although if the cinder rather than the vegetation were the objective, a better filter might have been chosen. The following are desirable for maximizing the potential of and simplifying aerial photography:

(1) Preflight albedo studies on the major rock types to intelligently recommend the best film and filter combinations.

(2) Separate photographic runs to produce scales which are directly comparable with other imaging sensors and with existing map coverage.

B. Infrared Imagery

Because of the ability to measure thermal diffusivity and albedo quantitatively, the dominant role of diffusivity in controlling infrared temperatures has become clear. With a few ground calibration points, it should be possible to infer diffusivity and albedo characteristics of materials from day and night IR imagery. Further studies should be made on the effects of moisture and density on these thermal parameters. The following steps are advised to realize the full potential from IR imagery:

(1) Obtain albedos and thermal diffusivities of representative rock units.

(2) Make preflight thermal radiometer measurements, to select the optimum flight times.

(3) Take surface temperature measurements and collect rock and soil moisture data, at the times of overflights.

C. Scatterometry

The radar scatterometer can yield valuable information on surface roughness, particle size and topography. Because of the problems of data reduction, the full potential of this system has not yet been realized. Topographic variations are best seen from distance-versus-return plots at each look angle whereas roughness data may be seen either as distance-versus-return plots or sigma curves, the latter being the best. Topographic variations make the sigma curves currently produced. over any but the flattest terrain, meaningless. Unless a system for inputting topographic information into computer reductions of sigma curves can be made, only distance-versus-return plots will be useful for geologic problems. From the distance-versus-return plots, selected sigma curves may be graphed after the individual plots are "slipped" to correct for topography. Because both distance-versus-return plots and sigma curves were hand reduced, only a few areas on the two runs were investigated thoroughly. The following are recommendations for future scatterometry flights over geologic targets:

(1) Provide for strict topographic control and bore sighting of the data if sigma curves are to be produced.

(2) Fly scatterometry only when accompanied by 60% overlap metric photography for topographic control.

(3) Collect particle size and roughness data on representative areas of terrain.

D. Microwave Radiometry

Significant steps were made toward understanding the microwave emission from geologic targets. Through field studies, quantitative measures of penetration depth were obtained for various materials. Also, a limited measure of the effect of water on penetration depth was obtained.

A graphic method of demonstrating roughness effects was proposed. A combination of ground-based and theoretical radiometer data was used for calibration of the aircraft microwave radiometers. While no new interpretations of the aircraft microwave data were made, the data collected for this year substantiated the previous results that the cinder and basalt were differentiable with the microwave radiometers.

This study points out clearly that a balanced effort between ground-based and aircraft oriented studies is absolutely essential in relating microwave emission to geologic phenomena. An understanding of the basic phenomena, such as penetration depth, moisture effects, and density dependencies, can be most expeditiously obtained by means of well controlled ground-based experimentation. On the other hand, airborne sensors are indispensable in obtaining rapid, synoptic coverage of an area, graphically demonstrating the differences or similarities between varying units at a particular point in time.

The following criteria are listed as being desirable in obtaining ground-based data for calibration or comparison with aircraft data:

(1) Use identical radiometric systems.

(2) View the same target.

(3) View representative samples.

(4) View a large homogeneous area.

(5) Arrange an identifiable point in the data or in time on the data.

(6) Perform the measurements concurrently.

It is the conclusion of this paper that ground-based studies should be performed on a continuing basis, especially concurrently with aircraft overflights. Study of the following areas is recommended:

(1) Relation of penetration depth and emissivity to water content.

(2) Relation of penetration depth and emissivity to density.

(3) Relation of emissivity to roughness.

(4) Items (1), (2), and (3) above for different, representative materials.

(5) Roughness phase diagraming for different materials to determine its potential as a roughness classifier.

(6) Experiments to determine if the presence of water enhances geologic features, especially subsurface, in the multispectral microwave signatures.

References

1. Blinn, J. C., Chapman, P., and Quade, J., *Airborne Multifrequency Microwave Radiometric Sensing of an Exposed Volcanic Province,* Technical Memorandum 33-405. Jet Propulsion Laboratory, Pasadena, Calif., Oct. 15, 1968.
2. Conel, J. E., *Microwave Emission From Granular Silicates: Determination of the Absorption Coefficient From Plate Measurements,* Technical Memorandum 33-458. Jet Propulsion Laboratory, Pasadena, Calif.
3. Marandino, G. E., *Microwave Signatures from Various Terrain,* B.S. Thesis. Massachusetts Institute of Technology, Cambridge, Mass., May, 1967.
4. Beckman, P., and Spizzichino, A., *The Scattering of Electromagnetic Waves from Rough Surfaces.* Pergamon Press, New York, 1963.

NASA — JPL — Coml., L.A., Calif.